1

Fundamentals of Fracture Mechanics

1.1 Introduction and Historical Background

Classical fracture mechanics is a direct application of classical continuum mechanics. It introduces a length parameter into structural assessment known as the size of an existing defect or the crack length. Thus, fracture mechanics is based on the existence of an initial crack and subsequent crack propagation under cyclic loading. An important aspect in the development of classical fracture mechanics is the principle of *locality* of the state distribution of stresses. Fatigue crack propagation analyzed with fracture mechanics enables us to quantify the residual lifetime of a cracked component. It requires a combined background of analytical solid mechanics, material science, probability theory, and catastrophe theory¹ to calculate the load and stress in structural components.

The solution for the stress distribution around a circular hole in a much larger plate under remotely uniform tensile stress was derived by Kirsch (1898). The solution for stresses around an elliptical hole was independently derived by Kolosov (1909) and Inglis (1913). Their solution showed that the concentration of stress could become far greater as the radius of curvature at one end of the hole becomes small compared to the overall length of the hole. The elliptical hole of Kolosov and Inglis defines a crack in the limit when one semi-axis goes to zero. The Inglis solution was adopted by Griffith (1921) to describe a crack in a brittle solid. Griffith made his famous criterion that spontaneous crack growth would occur when the energy released from the elastic field is in balance with the work required to separate surfaces in the solid.

According to Cotterell (2002), the first known works devoted to fracture mechanics were the two seminal papers of Griffith (1921, 1924). Griffith was motivated by the need to understand the effect of scratches on fatigue. It was originally thought that it should be possible to estimate the fatigue limit of a scratched component by using either the maximum principal stress criterion, favored by Lamé and Rankine, or the maximum principal strain criterion, favored by Ponclet and Saint-Venant. Griffith showed that scratches could increase the stress and strain level by a factor of between two and six. However, Griffith noted that the maximum stress or strain would be the same on a shaft

¹ Catastrophe theory is a branch of bifurcation theory in the study of dynamical systems (Thompson, 1982). A catastrophic failure is a sudden and total failure of a structure or system from which recovery is impossible. Catastrophic failures often lead to cascading systems failure.

of diameter 1 inch whether the scratches were one ten thousandth or one hundredth of an inch deep, provided they were geometrically similar. These conclusions were found to be in conflict with the fatigue results and led Griffith to reject the commonly held criteria of rupture. Wieghardt (1907) had earlier rejected these strength criteria for a different reason, but dealt with the paradox that the stresses at the tip of a sharp crack in an elastic body are infinite no matter how small the applied stress. This fact led him to argue that rupture does not occur when the stress at a point exceeds some critical value, but only when the stress over a small portion of the body exceeds a critical value. Taylor (1965) stated that Griffith was also aware of the paradox.

Griffith (1921) adopted energy concepts and realized that a certain minimum work was necessary to produce a fracture, which for an ideal elastic material was the surface free energy. Griffith realized that the fracture problem is an extension of the elastic theory of minimum potential energy. Griffith's global treatment of the energy balance for a cracked body was described by Taylor (1965) as "the first real advance in understanding the strength of materials." The practical importance of Griffith's work lies in his realization that the critical stress depends on a length scale, which is taken as the crack length. Griffith (1921) performed his experiments on a model made of glass material. From his experiments, he estimated the theoretical strength of glass to be about 2 GPa. The observed tensile strength of glass was 170 MPa. Hence Griffith predicted that there were flaws of the order of 5 µm. Griffith believed that the weakness of glass was due to internal flaws, and indeed believed that the surface layers might be of superior strength because flaws would be oriented parallel to the surface (Griffith, 1921). Later, Griffith (1924) stated that the "weakness (in pure silica) is due almost entirely to minute cracks in the surface, caused by various abrasive actions to which the material has been accidentally subjected after manufacture." Griffith's evidence was that if a strong silica rod was rubbed lightly with any other solid, it immediately loses its strength. However, he did not state that the weakness in glass was due to surface flaws. Joffé (1928) assumed that surface flaws are responsible for the weakness in glass. Joffé (1924) indicated that the strength of rock salt was due to surface flaws because when the surface layer was dissolved in warm water the strength increased.

The separation across a surface flaw in glass was found of the order 50 nm. The experiments on mica² conducted by Orowan (1933) proved that the reduction in strength was due to flaws. The usual tensile strength of mica has a value within the range 200–300 MPa but Orowan (1933) found that the strength is more than 3 GPa by stressing only the central strip of a mica sheet using grips that were much narrower than the sheet. The small value of the usual tensile strength of mica is due to the presence of cracks at the edge of the sheet. The first direct evidence for the existence of surface flaws in glass came by chance during experiments conducted on the properties of thin films of metal by Andrade and Martindale (1935). Later, Andrade and Martindale (1937) conducted another series of experiments on various glasses using sodium from a vapor to "decorate" the surface cracks. The reversibility of fracture was experimentally demonstrated by Obreimoff (1930) who studied the fracture of mica using a stable geometry. A glass wedge was used to cleave thin lamellar of mica of

² The mica group of sheet silicate (phyllosilicate) minerals includes several closely related materials. It has a very pronounced cleavage plane, and almost atomically perfect surfaces can be produced by cleavage.

thickness 0.1-0.2 mm from a block of mica. It was found that a crack could grow under the combined effect of mechanical energy and moisture in the air, and demonstrated the reversibility of fracture.

The transition temperature from ductile to brittle behavior in structural steel was found to be about 20 °C. In riveted structures, brittle fractures rarely caused catastrophes because a fracture was usually arrested at the edge of the plate. Brittle fracture in steel was studied in a 75 m high by 5 m diameter water standpipe at Gravesend, Long Island, NY in 1898 (SSC-65, 1953). Without proper fracture control, it is known that welding may cause brittle fracture in steel. In addition, it introduces high residual stresses equal to the yield strength, a heat affected zone adjacent to a weld with a much higher transition temperature than the parent plate, and crack-like defects. Unstable brittle fracture can easily run through a major part of its section. The first brittle fracture in a large welded structure occurred just before World War II in the Vierendeel Truss Bridge in Hasselt, Belgium, followed by failures in similar Belgium bridges during the war (SSC-65, 1953). Extensive studies of brittle fracture were initiated following the widespread fractures in the welded Liberty ships. There were 145 structural failures in Liberty ships where either the vessel was lost or the hull was so weakened as to be dangerous; a further 694 ships suffered major fractures requiring immediate repair (Biggs, 1960). The size effect on the brittle fracture of steel laboratory specimens was considered by Biggs (1960). Size effect was recognized by Docherty (1932), Irwin (1948), and Shearin et al. (1948). Plates of thickness ¾ in and up to 72 in wide were tested using a 3,000,000 lb hydraulic testing machine (SSC-3, 1946).

Several attempts were made to determine the transition temperature at which the fracture behavior changes from ductile to cleavage. For example, Ludwik (1909) considered the phenomenological transition from ductile to cleavage behavior, and proposed that the cohesive strength was little affected by temperature, but there was a marked increase in the yield strength of low carbon steel as the temperature decreased, so that at a particular temperature, cleavage fracture became easier than yielding. The effect of a notch on the transition temperature was considered to be primarily due to a constraint on yielding. Orowan (1945) used Ludwik's concept and showed that a notch would increase the transition temperature. The Charpy test (Charpy, 1912) is considered as one of the original and the most lasting of the small scale notch bend tests to assess the transition temperature in steel.

The first fracture test that fully simulated a welded plate structure was reported by Wells (1956a, 1956b, 1962) who designed a 600 ton testing machine capable of testing 1 in thick 36×36 in butt-welded plates. The welded plates could be tested either as welded or after heat treatment and were welded into the test rig. The plates were cooled with dry-ice to the desired temperature before testing. Those plates welded with rutile electrodes tended to have pre-cracks at the saw cut. Fractures were often initiated in pre-cracked specimens at low stress, or occurred spontaneously on cooling, and these arrested at the edge of the tensile residual stress zone along the weld (Wells, 1961). The transition from high stress fractures at the yield strength to low stress fractures did not always occur at the Charpy transition temperature.

This brief historical account constitutes the early state of the theory of fracture mechanics. Over time, this theory has been advanced by the contributions of many researchers. Generally, the theory of fracture mechanics is divided into linear elastic fracture mechanics (LEFM) and elasto-plastic fracture mechanics (EPFM). LEFM is convenient for brittle-elastic materials such as low-carbon steel, stainless steel, certain aluminum alloys and polymers. Note that plasticity always precedes fracture. The linear theory (LEFM) is governed by a parameter called the stress intensity factor, which determines the entire crack tip stress field and measures the material toughness (Rice, 1972). As indicated by Broek (1994), materials with relatively low fracture resistance fail below their collapse strength and can be analyzed on the basis of LEFM. On the other hand, if fracture is accompanied by considerable plastic deformation, the EPFM is used. The fracture parameters used in EPFM are referred to as the *J*-integral, which measures the strain energy release rate,³ and the *crack tip opening displacement* (CTOD). It should be noted that the present state of classical fracture mechanics has been promoted by the contribution of numerical methods, which have been developed to meet the demands of understanding the experimentally observed phenomena of fracture, and to transfer fracture mechanics material parameters to structural behavior. An extensive historical account of fracture mechanics and its development is documented by Brocks and Schwalbe (2016). For a detailed account, the reader may consult those references addressing different issues of fracture mechanics (e.g. Broek, 1974, 1994; Hutchinson, 1979; Lawn, 1993; Anderson, 1995; Wang, C.H., 1996; Farahmand et al., 1997; Liu, A.F., 1998; Tada et al., 2000; Buckley, 2005; Zehnder, 2007; Gross and Seeling, 2011; Schreurs, 2011).

This chapter begins with an introduction to the classical theory of continuum mechanics, which establishes the states of stress that will cause a particular material to fail. This is followed by introducing the stress intensity factor, which is usually used to determine the stress state near the tip of a crack for three linearly independent cracking modes. Methods of evaluating the stress intensity factor using analytical, experimental, or numerical approaches will be discussed. The linear elastic fracture mechanics (LEFM) will be introduced in terms of Griffith's criterion. This is followed by the nonlinear fracture mechanics (EPFM), which covers Irwin's criteria, crack tip element method, Paris–Erdogan law nonlinear fracture mechanics, and the *J-, M-, L,* and *L*-integrals. Because of its importance, the AFGROW (Air Force Grow), which is a damage tolerance analysis framework developed by the Air Force Research Laboratory, will be briefly outlined. Since layered structural elements may suffer from severe stress concentrations of an interlaminar character, the boundary-layer effect of composite structures together with the thermal loading stress field will be introduced. The chapter will close with conclusions and closing remarks.

1.2 Classical Theory of Solid Mechanics

The principle of *locality* states that a material point is only directly influenced by, and interacts with, its immediate surroundings. Accordingly, the stress state at a point depends on the deformation at that point only. The resulting crack growth criterion is referred to as *local*, because attention is focused on a small material volume at the crack tip. The classical theory of continuum mechanics is based on partial differential

³ Note that the term "rate" does not refer to derivative with respect to time. In this context, it refers to derivative with the size of the crack.

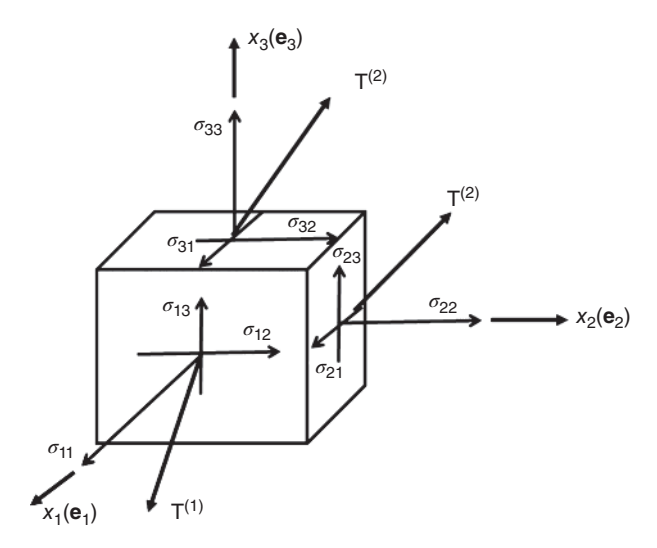


Figure 1.1 Cartesian components of the stress vector $T^{(j)}$, j = 1, 2, 3 acting on the three faces of the cubic elemental volume dV.

equations whose partial derivatives are continuous. Figure 1.1 shows nine stress components at each point of the medium. These stress components are dependent on position and time, i.e. $\sigma_{ij} = \sigma_{ij}(x, t)$. The unit vectors \mathbf{e}_1 , \mathbf{e}_2 , and \mathbf{e}_3 are established along the three Cartesian coordinates x_1 , x_2 , and x_3 , respectively. The stress vector $T^{(j)}$, j = 1, 2, 3, can be written in the form

$$\mathbf{T}^{(j)} = \sigma_{j1}\mathbf{e}_1 + \sigma_{j2}\mathbf{e}_2 + \sigma_{j3}\mathbf{e}_{13} \tag{1.1}$$

where e_1 , e_2 , and e_3 denote unit vectors along the coordinate axes 1, 2, and 3, respectively. The stress vector \mathbf{T} on a surface element with an outward normal \mathbf{n} can be expressed as a linear function of the stress σ_{ij} . For example the *j*-component of the stress vector **T** is

$$\sigma_{xx} = \frac{K_{II}}{\sqrt{2\pi r}} \sin\frac{\theta}{2} \left(2 + \sin\frac{\theta}{2}\sin\frac{3\theta}{2}\right) + ..., \sigma_{yy} = \frac{K_{II}}{\sqrt{2\pi r}} \left[\sin\frac{\theta}{2}\cos\frac{3\theta}{2}\cos\frac{3\theta}{2}\right] + ...$$

$$\tau_{xy} = \frac{K_{II}}{\sqrt{2\pi r}} \cos\frac{\theta}{2} \left(1 - \sin\frac{\theta}{2}\cos\frac{3\theta}{2}\right) + ...$$
(1.2)

We can write

$$\mathbf{T} = \sum_{j=1}^{3} T_{j} \mathbf{e}_{j} = \sum_{j=1}^{3} \left(\sum_{i=1}^{3} n_{i} \sigma_{ij} \right) \mathbf{e}_{j}$$
(1.3)

The Cauchy stress is given by the nine components

$$\sigma = \begin{bmatrix} \sigma_{11} & \sigma_{12} & \sigma_{13} \\ \sigma_{21} & \sigma_{22} & \sigma_{23} \\ \sigma_{31} & \sigma_{32} & \sigma_{33} \end{bmatrix} = \begin{bmatrix} \sigma_{xx} & \sigma_{xy} & \sigma_{xz} \\ \sigma_{yx} & \sigma_{yy} & \sigma_{yz} \\ \sigma_{zx} & \sigma_{zy} & \sigma_{zz} \end{bmatrix}$$
(1.4)

The linear momentum principle requires that we set to zero the limit over the closed surface *S*, i.e. $\lim_{S\to 0} (1/S) \int_{S} \mathbf{T} dS = 0$.

In applying the linear momentum principle to an arbitrary finite body, the divergence theorem of multivariable calculus shows that integrals over the area of a closed surface S, may be rewritten as integrals over the volume V enclosed by the surface S,

$$\int_{S} T_{j} dS = \int_{S} \left(n_{1} \sigma_{1j} + n_{2} \sigma_{2j} + n_{3} \sigma_{3j} \right) dS = \int_{V} \left(\frac{\partial \sigma_{1j}}{\partial x_{1}} + \frac{\partial \sigma_{2j}}{\partial x_{2}} + \frac{\partial \sigma_{3j}}{\partial x_{3}} \right) dV$$
(1.5)

In order to determine the equations of motion of an elemental volume of the body material consider a small cube of material of side length L centered on some arbitrary chosen point **x** and the forces along the x_1 axis as shown in Figure 1.2. The total body force is f_1L^3 . In the limit as $L \to 0$, upon expanding the stresses in a Taylor series and writing down Newton's second law, gives

$$\left(\frac{\partial \sigma_{11}}{\partial x_1} + \frac{\partial \sigma_{21}}{\partial x_2} + \frac{\partial \sigma_{31}}{\partial x_3}\right) L^3 + HOT + f_1 L^3 = \rho L^3 \mathbf{a}_1 \tag{1.6}$$

where a_1 is the acceleration along the x_1 axis and HOT denotes higher order terms. Canceling L^3 on both sides gives

$$\left(\frac{\partial \sigma_{11}}{\partial x_1} + \frac{\partial \sigma_{21}}{\partial x_2} + \frac{\partial \sigma_{31}}{\partial x_3}\right) + f_1 = \rho a_1$$
(1.6a)

The other two equations along x_2 and x_3 axes can be obtained in a similar way in the form

$$\left(\frac{\partial \sigma_{12}}{\partial x_1} + \frac{\partial \sigma_{22}}{\partial x_2} + \frac{\partial \sigma_{32}}{\partial x_3}\right) + f_2 = \rho \mathbf{a}_2, \left(\frac{\partial \sigma_{13}}{\partial x_1} + \frac{\partial \sigma_{23}}{\partial x_2} + \frac{\partial \sigma_{33}}{\partial x_3}\right) + f_3 = \rho \mathbf{a}_3 \tag{1.6b,c}$$

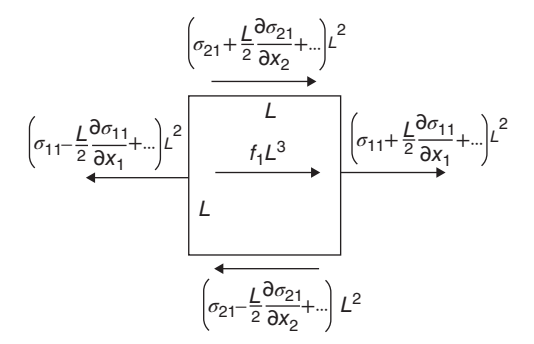


Figure 1.2 Forces acting along the x_1 -axis on a cube of side length L. Stresses around the cube faces are developed in a Taylor series expansion about their values at x.

For plane strain in which all displacements take place in one plane, and in the absence of body forces, the static equilibrium equations (zero inertia forces) are

$$\frac{\partial \sigma_{11}}{\partial x_1} + \frac{\partial \sigma_{21}}{\partial x_2} = 0 \quad \frac{\partial \sigma_{12}}{\partial x_1} + \frac{\partial \sigma_{22}}{\partial x_2} = 0 \tag{1.7a,b}$$

together with the strain compatibility equation

$$\frac{\partial^2 \varepsilon_{22}}{\partial x_1^2} + \frac{\partial^2 \varepsilon_{11}}{\partial x_2^2} = 2 \frac{\partial^2 \varepsilon_{12}}{\partial x_1 \partial x_2} \tag{1.8}$$

By using the stress-strain relations, the equilibrium equation takes the form

$$\nabla^2 \left(\sigma_{11} + \sigma_{22} \right) = 0 \tag{1.9}$$

Introducing the Airy stress function $\Phi = \Phi(x_1, x_2)$, which satisfies the plane stress in the absence of body forces, gives

$$\sigma_{11} = \frac{\partial^2 \Phi}{\partial x_2^2}, \quad \sigma_{12} = -\frac{\partial^2 \Phi}{\partial x_1 \partial x_2}, \quad \text{and} \quad \sigma_{22} = \frac{\partial^2 \Phi}{\partial x_1^2}$$
 (1.10)

Satisfying the strain compatibility and expressing the strains in terms of stresses by the linear isotropic relations gives

$$\nabla^2 \left(\sigma_{11} + \sigma_{22}\right) = \nabla^2 \left(\nabla^2 \Phi\right) = 0 \tag{1.11}$$

where $\nabla^2 = \frac{\partial^2}{\partial x_2^2} + \frac{\partial^2}{\partial x_2^2}$. Equation (1.11) is the known bi-harmonic equation.

Before establishing Griffith's criterion, consider first a circular hole of radius a in a plate whose dimensions are much larger than a and can, for present purposes, be taken as infinite as shown in Figure 1.3. The plate is subjected to a uniform stress σ^{∞} in the x_2 direction and the boundary of the hole is free of loading. The solution of equation (1.11) was developed to satisfy the conditions $\sigma_{22} \to \sigma$ and $\sigma_{11} \to 0$ as $r \to 0$, and that $\sigma_r = \sigma_{r\theta} = 0$ at r = a. To establish a unique solution, we have to specify the value of the integral of $\partial \mathbf{u} / \partial s$, where \mathbf{u} is the deformation displacement vector, and s is the arc length around the hole. This integral is zero in the present case for which a single-valued displacement field is required. It is non-zero if the hole was to represent the core of a dislocation. Accordingly, the solution may be written in the form $\Phi = g(r) + h(r)\cos 2\theta$, with the functions g(r) and h(r) written the form $h(r) = C_4 r^4 + C_2 r^2 + C_0 + C_{-2} r^{-2}$. The constants C_i are obtained from the conditions on the stress at r = a and $r \to \infty$ to give single-valued displacements. The solution for Φ is given by the following expressions for the stresses

$$\sigma_{rr} = \frac{\sigma}{2} \left[\left(1 - \frac{a^2}{r^2} \right) - \left(1 - 4 \frac{a^2}{r^2} + 3 \frac{a^4}{r^4} \right) \cos 2\theta \right],$$

$$\sigma_{r\theta} = -\frac{\sigma}{2} \left(1 + 2 \frac{a^2}{r^2} - 3 \frac{a^4}{r^4} \right) \sin 2\theta$$

$$\sigma_{\theta\theta} = \frac{\sigma}{2} \left[\left(1 + \frac{a^2}{r^2} \right) + \left(1 + 3 \frac{a^4}{r^4} \right) \cos 2\theta \right]$$
(1.12)

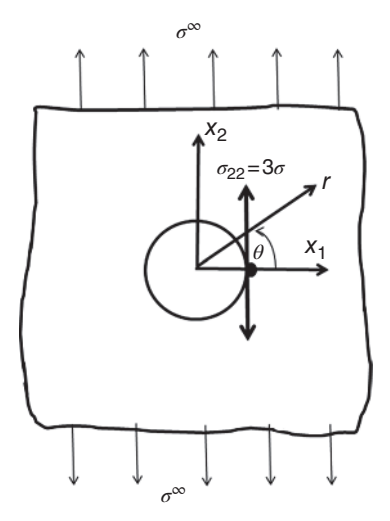


Figure 1.3 Large plate with a circular hole circular tunnel under remote tensile stress.

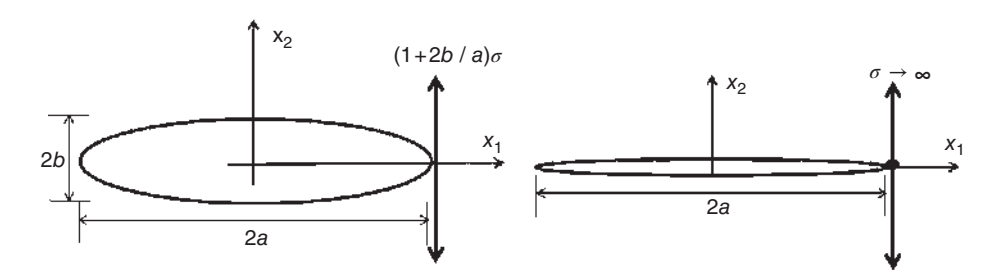


Figure 1.4 (a) Elliptic hole and (b) the limit to a flat crack of width 2a.

Equations (1.12) reveal that at r=a, $\sigma_{\theta\theta}=\sigma\left(1+2\cos2\theta\right)$. Of particular interest are the values of the stresses at the special points: $\sigma_{\theta\theta}\mid_{\theta=0,\,\pi}=\sigma_{22}=3\sigma$, and $\sigma_{\theta\theta}\mid_{\theta=\pi/2,\,-\pi/2}=\sigma_{11}=-\sigma$. Thus it is expected that failure would begin at $\theta=0$ or π in a brittle material under remote tensile loading.

If the hole is an elliptic cavity, as shown in Figure 1.4(a), with major and semi-axes a and b, respectively, then the concentration of stress at points of the hole boundary intersected by the x_1 axis is

$$\sigma_{22} = \left(1 + \frac{2b}{a}\right)\sigma = \left(1 + 2\sqrt{a/\rho_{tip}}\right)\sigma\tag{1.13}$$

where $\rho_{tip} = b^2/a$ is the radius of curvature of the hole boundary at $x_1 = \pm a$. Note that the stress induced along the hole boundary where it is intersected by the x_2 axis is $\sigma_{11} = -\sigma$. With reference to a flat crack lying along the x_1 axis with $-a < x_1 < +a$ as shown in Figure 1.4(b), the stress concentration at the hole results in singularity. To demonstrate this singularity with the linear theory, the crack opening gap $\Delta u_2 = u_2^+ - u_2^-$,

where + and - denotes the upper and lower crack surfaces, may be given by the expression (Rice, 2010)

$$\Delta u_2 = \frac{4\sigma}{E} \sqrt{a^2 - x_1^2}, \quad -a < x_1 < +a \tag{1.14}$$

The tensile stress transmitted across the x_1 axis outside the crack is

$$\sigma_{11} = \frac{\sigma |x_1|}{\sqrt{x_1^2 - a^2}} \text{ over the ranges } -\infty < x_1 < a \quad \text{and} \quad +a < x_1 < +\infty$$
 (1.15)

Relations (14) and (15) reveal that at $x_1 = a$ the displacement of the crack walls is proportional to $\sqrt{a^2 - x_1^2}$; on the other hand, the stress at a small distance ahead of the crack is proportional to $1/\sqrt{x_1^2-a^2}$. In linear elasticity, it is well known that stress singularities are prevalent at the corners of geometric boundaries joining dissimilar materials (e.g. Bogy, 1968; Hein and Erdogan, 1971; Kuo and Bogy, 1974).

The problem of predicting states of stress that will cause a particular material to fail plays an important role in the design of structural components. Many fractures are appropriately described as being partially brittle and partially ductile, meaning that certain portions of the fractured surface are approximately aligned with planes of maximum shear stress, while others appear granular, as in the case of brittle fracture and are oriented more toward planes of maximum tensile stress. The design and development of structural systems generally involves biaxial (occasionally triaxial) stresses covering a wide range of ratios of principal stresses. In the simple classical theories of failure, it is assumed that the same amount of whatever caused the selected tensile specimen to fail will also cause any part made of the materials to fail regardless of the state of stress involved (Wolf et al., 2003). In the area of structural mechanics, the following stress/strain theories are very useful:

Maximum normal stress theory (Rankine) is the simplest of the various theories; it states merely that a material subjected to any combination of loads will experience:

- 1) yield, whenever the greatest positive principal stress exceeds the tensile yield strength in a simple uniaxial tensile test of the same material, or whenever the greatest negative principal stress exceeds the compressive yield strength,
- 2) fracture, whenever the greatest positive (or negative) principal stress exceeds the tensile (or compressive) ultimate strength in a simple uniaxial tensile (or compressive) test of the same material.

Maximum shear stress theory (also known as the Coulomb or Tresca theory) states that a material subjected to any combination of loads will fail (by yielding or fracturing) whenever the maximum shear stress exceeds the shear strength (yield or ultimate) in a simple uniaxial stress test of the same material (Wolf et al., 2003).

Maximum normal-strain theory (Saint-Vanent's theory) states that failure will occur whenever a principal normal strain reaches the maximum normal strain in a simple uniaxial stress test of the same material.

1.3 Stress Intensity Factor

1.3.1 Analytical Development

The stress intensity factor is usually used to determine the stress state near the tip of a crack. It is applied to homogeneous linear elastic material. It is useful to provide a failure criterion for brittle materials. Figure 1.5 shows that the crack tip polar coordinates such that $\theta=0$ is taken as the direction of the crack growth and $\theta=\pm\pi$ denotes the crack walls. The crack tip field was described by Williams (1952, 1957) and (Rice (2010) who set $\partial/\partial t=-V_{cr}\partial/\partial x_1$, where V_{cr} is the instantaneous speed of crack propagation, to determine the Airy stress function Φ such that $\sigma_{r\theta}=\sigma_{\theta\theta}=0$ at the crack walls. The solution for Φ was assumed in the form

$$\Phi = r^{\lambda+2} \Big[A\cos \lambda \theta + B\cos ((\lambda + 2)\theta) \Big]$$
(1.16)

where A, B, and $\hat{\chi}$ are constants. The symmetry part of the Airy stress function requires that $\sigma_{r\theta} = \sigma_{\theta\theta} = 0$ at the crack walls. In other words, the form of the Airy function should result in stresses proportional to $r^{\hat{\lambda}}$ (with values $\hat{\chi}$ being multiple of ½). The stresses are:

$$\sigma_{\theta\theta} = \frac{\partial^2 \Phi}{\partial r^2} = (\hat{\lambda} + 2)(\hat{\lambda} + 1)r^{\hat{\lambda}} \left[A\cos \hat{\lambda}\theta + B\cos((\hat{\lambda} + 2)\theta) \right]$$
(1.17a)

$$\sigma_{r\theta} = -\frac{\partial}{\partial r} \left(r^{-1} \partial \Phi / \partial \theta \right) = (\lambda + 1) r^{\lambda} \left[A \hbar \sin \hbar \theta + B (\hbar + 2) \sin \left((\hbar + 2) \theta \right) \right]$$
 (1.17b)

At $\theta = \pm \pi$, we have $\sigma_{\theta\theta} = \sigma_{r\theta} = 0$, which gives $(A+B)\cos \lambda \pi = [A\lambda + (\lambda + 2)B]\sin \lambda \pi = 0$. This condition gives $\lambda = ..., -3/2, -1/2, 1/2, 3/2, ...$ with $B = -A\lambda(\lambda + 2)$. Also $\lambda = ..., -3, -2, -1, 0, 1, 2, 3, ...$ with B = -A. We have to reject all negative values

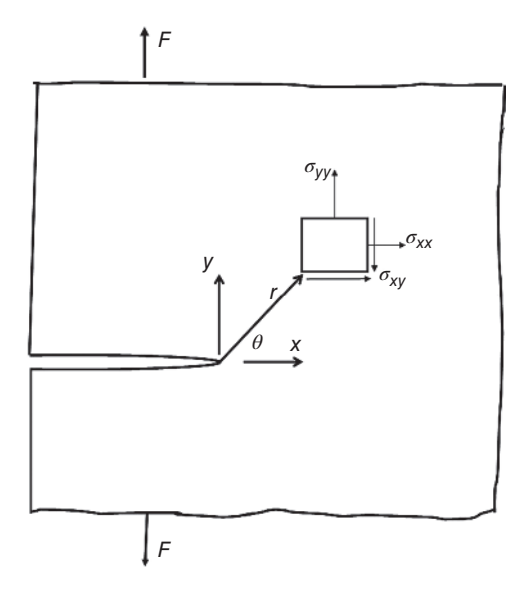


Figure 1.5 Crack tip coordinates for establishing the stress intensity factor.

of λ , as they would lead to unbounded total strain energy of some finite region and so only the values $-1 < \lambda < 0$ are admissible and allow a singular field meeting the crack surface boundary conditions. For $\hat{\lambda} = -1/2$, B must be related to A. Thus the singular field at the crack tip has one free parameter A which is redefined as $1/\sqrt{2\pi}$ times a parameter designated by K_I . The singular distribution of stress at a tensile crack tip is then found in the form:

$$\sigma_{\theta\theta} = \frac{K_I}{\sqrt{2\pi r}} \cos^3\left(\frac{\theta}{2}\right), \ \sigma_{\theta r} = \frac{K_I}{\sqrt{2\pi r}} \cos^2\left(\frac{\theta}{2}\right) \sin\left(\frac{\theta}{2}\right), \ \sigma_{rr} = \frac{K_I}{\sqrt{2\pi r}} \cos\left(\frac{\theta}{2}\right) \left[2 - \cos^2\left(\frac{\theta}{2}\right)\right]$$
 (1.18)

where K_I is referred to as the mode-I *stress intensity factor*, which is proportional to the loading and depends on crack geometry, and gives the stress acting across the plane $\theta = 0$ very near to the crack tip.

Irwin (1957, 1958) determined the amount of energy available for fracture in terms of the asymptotic stress and displacement fields around a crack front in linear elastic solids. This asymptotic expression for the stress field near a crack tip is given in terms of polar coordinates, r, θ as

$$\sigma_{ij} \approx \left(\frac{K}{\sqrt{2\pi r}}\right) f_{ij}(\theta) + \text{higher order terms}$$
 (1.19)

where σ_{ii} are the Cauchy stresses, r is the distance from the crack tip, θ is the angle with respect to the plane of the crack, and f_{ii} are (non-dimensional) functions that are dependent on the geometry and loading conditions (see Figure 1.5). Irwin called the quantity K as the *stress intensity factor*. It is seen that equation (1.19) involves singularity close to the tip as $r \to 0$. Since the quantity f_{ij} is dimensionless, the stress intensity factor can be expressed in units of stress $\times \sqrt{\text{length}}$.

Three linearly independent cracking modes are used in fracture mechanics, usually referred as mode-I, -II, or -III, as shown in Figure 1.6. Mode-I is an opening (tensile) mode where the crack surfaces move directly apart. Mode-II is a sliding (in-plane shear) mode where the crack surfaces slide over one another in a direction perpendicular to the leading edge of the crack. Mode-III is a tearing (anti-plane shear) where the crack surfaces move relative to one another and parallel to the leading edge of the crack. With reference to Figure 1.5, the detailed expressions of σ_{ij} in the absence of constraint are as follows (Broek, 1994; Fett, 1998).

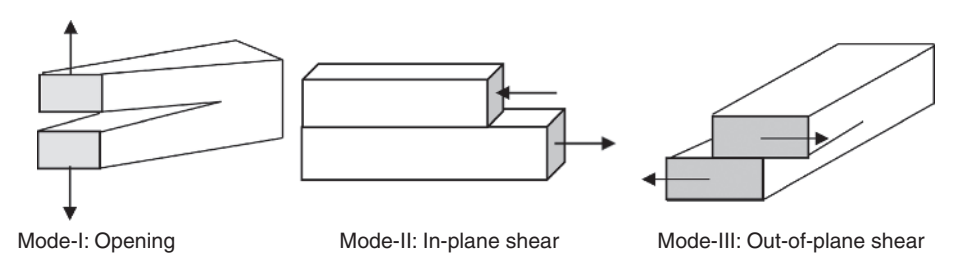


Figure 1.6 Modes of crack loading.

Mode-I (opening mode):

$$\sigma_{xx} = \frac{K_I}{\sqrt{2\pi r}} \cos \frac{\theta}{2} \left(1 - \sin \frac{\theta}{2} \sin \frac{3\theta}{2} \right) + \dots, \quad \sigma_{yy} = \frac{K_I}{\sqrt{2\pi r}} \cos \frac{\theta}{2} \left(1 + \sin \frac{\theta}{2} \sin \frac{3\theta}{2} \right) + \dots$$

$$\sigma_{zz} = 0, \quad \tau_{xy} = \frac{K_I}{\sqrt{2\pi r}} \left[\cos \frac{\theta}{2} \sin \frac{\theta}{2} \cos \frac{3\theta}{2} \right] + \dots$$

$$(1.20)$$

Mode-II (sliding mode): For this mode anti-symmetry of the tangential displacement component and boundary conditions for the crack face stresses allow the determination of the integration constants:

$$\sigma_{xx} = \frac{K_{II}}{\sqrt{2\pi r}} \sin\frac{\theta}{2} \left(2 + \sin\frac{\theta}{2} \sin\frac{3\theta}{2} \right) + \dots, \quad \sigma_{yy} = \frac{K_{II}}{\sqrt{2\pi r}} \left[\sin\frac{\theta}{2} \cos\frac{\theta}{2} \cos\frac{3\theta}{2} \right] + \dots$$

$$\tau_{xy} = \frac{K_{II}}{\sqrt{2\pi r}} \cos\frac{\theta}{2} \left(1 - \sin\frac{\theta}{2} \cos\frac{3\theta}{2} \right) + \dots$$

$$(1.21)$$

Mode-III (out-of-plane shear): Only the out-of-plane displacement is relevant (Schreurs, 2011):

$$\sigma_{zx} = \frac{K_{III}}{\sqrt{2\pi r}} \left[-\sin\frac{\theta}{2} \right], \quad \sigma_{zy} = \frac{K_{III}}{\sqrt{2\pi r}} \left[\cos\frac{\theta}{2} \right], \quad u_{zz} = \frac{2K_{III}}{\mu} \sqrt{\frac{r}{2\pi}} \left[\sin\frac{\theta}{2} \right]$$
(1.22)

where $\mu = \frac{E}{2(1+\nu)}$, E and ν are Young's modulus and Poisson's ratio, respectively.

Note that the first term in the series of equations (1.20) is the dominant term close to the crack tip. This term represents the singularity of the stress field, because it becomes infinite when approaching the crack tip.

The stress intensity factors for the three loading modes shown in Figure 1.6 are denoted by K_I , K_{II} , and K_{III} . They are formally defined by the expressions (Rooke and Cartwright, 1976):

$$K_{I} = \lim_{r \to 0} \sqrt{2\pi r} \sigma_{yy}(r, 0), \quad K_{II} = \lim_{r \to 0} \sqrt{2\pi r} \sigma_{yx}(r, 0), \quad K_{III} = \lim_{r \to 0} \sqrt{2\pi r} \sigma_{yz}(r, 0)$$
 (1.23)

Mixed mode stress intensity factor may be expressed by the following expression in polar coordinates (Bower, 2012)

$$\sigma_{\theta\theta} = \frac{K_I}{\sqrt{2\pi r}} \left[\frac{3}{4} \cos\frac{\theta}{2} + \frac{1}{4} \cos\frac{3\theta}{2} \right] - \frac{K_{II}}{\sqrt{2\pi r}} \frac{3}{4} \left[\sin\frac{\theta}{2} + \sin\frac{3\theta}{2} \right]$$
(1.24a)

$$\sigma_{r\theta} = \frac{K_I}{\sqrt{2\pi r}} \frac{1}{4} \left[\sin\frac{\theta}{2} + \sin\frac{3\theta}{2} \right] + \frac{K_{II}}{\sqrt{2\pi r}} \left[\frac{1}{4} \cos\frac{\theta}{2} + \frac{3}{4} \cos\frac{3\theta}{2} \right]$$
(1.24b)

$$\sigma_{rr} = \frac{K_I}{\sqrt{2\pi r}} \left[\frac{5}{4} \cos \frac{\theta}{2} - \frac{1}{4} \cos \frac{3\theta}{2} \right] + \frac{K_{II}}{\sqrt{2\pi r}} \left[\frac{5}{4} \sin \frac{\theta}{2} + \frac{3}{4} \sin \frac{3\theta}{2} \right]$$
(1.24c)

The corresponding expressions in Cartesian coordinates are

$$\sigma_{xx} = \frac{K_I}{\sqrt{2\pi r}} \cos\frac{\theta}{2} \left[1 - \sin\frac{\theta}{2} \sin\frac{3\theta}{2} \right] - \frac{K_{II}}{\sqrt{2\pi r}} \sin\frac{\theta}{2} \left[2 + \cos\frac{\theta}{2} \cos\frac{3\theta}{2} \right]$$
(1.25a)

$$\sigma_{yy} = \frac{K_I}{\sqrt{2\pi r}} \cos\frac{\theta}{2} \left[1 + \sin\frac{\theta}{2} \sin\frac{3\theta}{2} \right] + \frac{K_{II}}{\sqrt{2\pi r}} \left[\sin\frac{\theta}{2} \cos\frac{\theta}{2} \cos\frac{3\theta}{2} \right]$$
(1.25b)

$$\sigma_{xy} = \frac{K_I}{\sqrt{2\pi r}} \sin\frac{\theta}{2} \cos\frac{\theta}{2} \cos\frac{3\theta}{2} + \frac{K_{II}}{\sqrt{2\pi r}} \cos\frac{\theta}{2} \left[1 - \sin\frac{\theta}{2} \sin\frac{3\theta}{2}\right]$$
(1.25c)

$$\sigma_{zx} = \frac{K_{III}}{\sqrt{2\pi r}} \left[-\sin\frac{\theta}{2} \right] \quad \sigma_{zy} = \frac{K_{III}}{\sqrt{2\pi r}} \left[\cos\frac{\theta}{2} \right]$$
 (1.25d,e)

The displacement components are obtained by integrating the strains with the result

$$u_x = \frac{K_I}{\mu} \sqrt{\frac{r}{2\pi}} \left[1 - 2\nu + \sin^2 \frac{\theta}{2} \right] \cos \frac{\theta}{2} + \frac{K_{II}}{\mu} \sqrt{\frac{r}{2\pi}} \left[2 - 2\nu + \cos^2 \frac{\theta}{2} \right] \sin \frac{\theta}{2}$$
 (1.26a)

$$u_{y} = \frac{K_{I}}{\mu} \sqrt{\frac{r}{2\pi}} \left[2 - 2\nu - \cos^{2}\frac{\theta}{2} \right] \sin\frac{\theta}{2} + \frac{K_{II}}{\mu} \sqrt{\frac{r}{2\pi}} \left[-1 + 2\nu + \sin^{2}\frac{\theta}{2} \right] \cos\frac{\theta}{2}$$
 (1.26b)

$$u_z = \frac{K_{III}}{\mu} \sqrt{\frac{2r}{\pi}} \sin\frac{\theta}{2} \tag{1.26c}$$

In addition to the stress intensity factor, there is experimental evidence that the stress contributions acting over a longer distance from the crack tip may affect fracture mechanics properties. The constant stress contribution (first "higher-order" term of the Williams stress expansion, denoted as the *T-stress term*) is the next important parameter. The T-stress term is independent of the distance from the crack tip (Fett, 2008). For remote stresses, the constant stress components $\tau_{xy, 0} = \tau_{yx, 0} = 0$, $\sigma_{yy, 0} = 0$, and the stress tensor reads

$$\sigma_{ij,0} = \begin{bmatrix} \sigma_{xx,0} & 0 \\ 0 & 0 \end{bmatrix} = \begin{bmatrix} T & 0 \\ 0 & 0 \end{bmatrix}$$
 (1.27)

where *T* is known as the *T-stress*.

The T-stress has been shown to play a significant role in crack growth under mixed-mode loading conditions, and also in crack path stability under pure mode-I loading conditions. Sufficient information about the stress state is available, if the stress intensity factor and the T-stress are known. In special cases, it may be advantageous to also know higher coefficients of the stress series expansion. This is desirable for the computation of stresses over a somewhat wider distance from a crack tip.

Evaluation of Stress Intensity Factors

Stress intensity factors depend on the geometry of the structural element and loading conditions (tension, bending, thermal stresses, etc.). The stress intensity factor is usually determined using analytical, experimental, or numerical approaches. Different methods of stress intensity factor determination are documented in Fett (1998), Fett and Munz (1997), and books by Sih et al. (1965), Sih (1973), Rooke (1986b), Tada et al. (2000), and Sanford (2003).

Analytical methods include conformal transformation, where a body is mathematically transformed into another geometry, for which the solution to the stress field is easier to obtain (Muskhelishvili, 1977). The body force method was proposed by Nisitani (1967) for problems with a simple geometry and loading. The problem was formulated as a system of singular integral equations, where the unknown function is the densities of body forces distributed in an infinite body.

The experimental methods include photoelastic determination of the mode-I stress intensity factor (Etheridge and Dally, 1977). This method cannot be used for twodimensional surface cracks as the measurement of stress intensity factor is performed at the surface. The method of caustics, 4 known as shadow-spot method (Kalthoff, 1987) and Rosakis and Ravi-Chandar, 1986), is an optical way of visualizing the stress distribution close to the crack tip. This method relies on deflection of light rays due to stress-field gradients. Since the in-plane stresses near the crack tip are both tensile, the Poisson effect causes a local contraction (or thinning) of the material in the out-of-plane direction, which itself acts as a divergent lens and deflects the light. This technique can only be used for edge or through one-dimensional cracks, with small-scale yielding at the crack tip. It was demonstrated that strain gauges can be used to give local values of strain, from which the stress field is then inferred (Dally and Sanford, 1987). Stress intensity factors obtained from thermo-elastic experiments were determined from the cyclic stress field ahead of a fatigue crack by Diaz et al. (2004). The idea of thermo-elastic experiments is based on the fact that a small change in temperature due to the deformation of the material at the crack tip region can be measured and used to evaluate the stress levels. The change in the compliance of the specimen was used to obtain the stress intensity factor, based on the work-energy approach (Gallaghar, 1971).

Numerical algorithms include the compounding methods in which the stress intensity factor for a complex geometry is obtained as the sum of a series of auxiliary problems (Cartwright and Rooke, 1974). The K value due to each of the geometrical features was determined independently, and the results were compounded, with the addition of an extra stress intensity value, which denotes the interaction of the different boundaries in terms of the stress intensity factor (Cartwright and Rooke, 1974; Rooke, 1986a). The effects of different independent loadings were added to obtain the combined effect. Other numerical approaches include the transform method (Sneddon and Lowengrub, 1969), the Laurent series expansion (Isida, 1971, 1973), the boundary collocation method, and the finite element method (Fett and Munz, 1997; Chahardehi, 2008). The boundary collocation method was used to determine the stress intensity factor from boundary stresses. If the stress-field disturbance due to a crack is confined to a small region away from the boundaries, its effect on the stresses at the boundaries would be negligible, and therefore undetectable by the boundary collocation method. On the other hand, the finite element method was used for evaluating the stress intensity factor

⁴ A caustic is the envelope of light rays reflected or refracted by a curved surface or object, or the projection of that envelope of rays on another surface. The caustic is a curve or surface to which each of the light rays is tangential, defining the boundary of an envelope of rays as a curve of concentrated light.

for practical purposes. It has two main advantages over the boundary collocation technique. The first is that a priori knowledge of the stress series solution is not needed for the interior of the body. The second is the availability of numerous finite element software packages that have been developed, with many capabilities.

Weight functions enable separation of the loading and geometry by considering the effect of each one of these two factors on the stress intensity factor separately. For example, weight functions for one-dimensional crack problems were considered by Chahardehi (2008). The idea of the weight function approach for calculating the stress intensity factor was explained by Büeckner (1970), who indicated that it generally computes the stress field in the unnotched specimen. Büeckner (1970) showed that for the one-dimensional crack problem, in which the crack is loaded symmetrically, the stress intensity factor can be expressed using a 'weight function', as

$$K = \int_{0}^{a} \sigma(x)h(a,x)dx \tag{1.28}$$

where $\sigma(x)$ is the stress on the crack surface plane in the uncracked body under the action of the same boundary and body forces, and h(a,x) is the weight function. It should be noted that the weight function is unique for a specific crack-specimen geometrical configuration and is not a function of the load (Büeckner, 1970; Rice, 1972). Rice (1972) showed that for any symmetrical load system leading to stress intensity factor K and displacement field **u**, the weight function can be expressed as

$$h(a,x) = \frac{H}{2K} \frac{\partial \mathbf{u}}{\partial a} \tag{1.29}$$

where *H* is an appropriate elastic modulus. For an isotropic material $H = E/(1-v^2)$ for plane strain, and for plane stress H = E. Sih et al. (1965) presented estimated H for anisotropic materials. Equation (1.29) implies that if the stress intensity factor value and the corresponding crack displacement are known under any arbitrary stress distribution, then by use of the weight function, the stress intensity factor for any other stress system acting on the same specimen can be calculated as:

$$K^{ii} = \int_{0}^{a} \sigma^{ii}(x) \frac{H}{2K^{i}} \frac{\partial \mathbf{u}^{i}}{\partial a} dx$$
 (1.30)

The stress intensity factor values for a large variety of crack-loadings are well documented in several references (e.g. Rooke, 1986b, Murakami, 1987, and Tada et al., 2000).

1.4 **Linear Elastic Fracture Mechanics (LEFM)**

The linear elastic material behavior is an essential assumption in the theory of linear elastic fracture mechanics. Linear elastic fracture mechanics (LEFM) deals with sharp cracks in elastic bodies and is applicable to any material as long as the material is elastic except in a vanishingly small region at the crack tip, brittle or quasi-brittle fracture, and stable or unstable crack growth. The prediction of crack growth in LEFM theory is based on the concept of energy balance as defined by Griffith's criterion.

1.4.1 Griffith's Criterion

Griffith (1921) developed a linear elastic fracture criterion for brittle materials. He recognized that the difference between the energy released (if a crack was extended) and the energy needed to create new surfaces would result in a force for crack extension. In other words, crack growth will occur when there is enough energy available to generate new crack surface. The *energy release rate* is an essential quantity in energy balance criteria. Figure 1.4(b) shows a cracked structure with a crack length 2a and subjected to uniaxial loading of stress σ . Griffith estimated the strain energy stored per unit thickness to be

$$U_e = -\frac{\pi a^2 \sigma^2}{E} \tag{1.31}$$

where *E* is Young's modulus of the material, and the minus sign indicates that this energy would be released from the material. The energy associated with the surface area of the crack per unit thickness is

$$U_s = 2(2a)\gamma \tag{1.32}$$

where γ is the material specific surface energy density (J/m²). Figure 1.7 shows the total energy associated with a crack, which is the sum of the positive energy absorbed to cause the new surface plus the negative strain energy released by allowing the regions near the crack flanks to become unloaded. Note that when the total crack energy reaches its maximum value the structures equilibrium condition becomes unstable and fracture of the structure will occur at the equilibrium condition. Griffith assumed that the crack will propagate under constant applied stress, σ , if an incremental increase in crack length produces no change in the total energy of the surface. In other words, the derivative of the total energy with respect to a vanishes, that is,

$$\frac{d}{da}\left[U_e + U_s\right] = 0\tag{1.33}$$

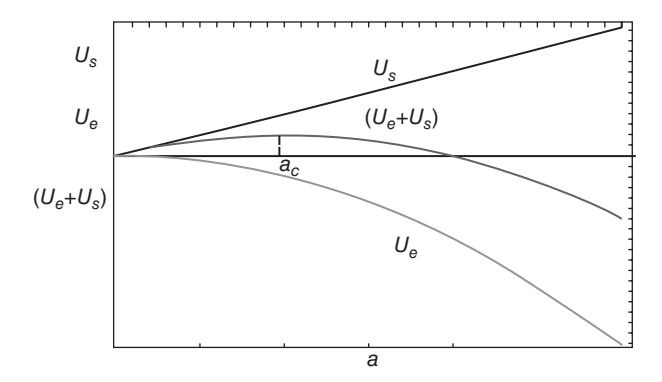


Figure 1.7 Dependence of strain energy (U_e), surface energy (U_s), and their sum of the crack length showing the critical crack length.

This condition results in the critical stress, σ_{cr} ,

$$\sigma_{cr} = \sqrt{\frac{2E\gamma}{\pi a_c}} \tag{1.34}$$

The corresponding critical crack length is a_c , which is shown in Figure 1.7. Condition (1.34) is known as the Griffith criterion, which states that the change of surface energy must be greater than the change of strain energy in order to maintain the integrity of a structural member. Beyond the critical crack length a_c the structure can lower its energy by letting the crack grow still longer.

The theory of linear elasticity predicts that the stress at the tip of a sharp flaw in a linear elastic material is infinite. To avoid this singularity, Griffith developed a thermodynamic approach to explain the observed relation. The growth of a crack requires the creation of two new surfaces and hence an increase in the surface energy. The capacity for Griffith's theory to predict crack growth was questioned by Francfort and Marigo (1998) due to its shortcomings in predicting the crack initiation, crack path, and crack jumps along the crack path. For this reason, they proposed a variational model of quasistatic crack evolution in line Griffith's theory of brittle fracture. However, their proposed model is not itself restricted by the usual constraints of that theory, which require a pre-existing crack and a well-defined crack path. In contrast, crack initiation and crack path can be quantified. The numerical implementation of the model of brittle fracture developed in Francfort and Marigo (1998) was employed by Bourdin et al. (2000). Various computational methods based on variational approximations of the original functional were proposed. They were tested on several anti-planar and planar examples that are beyond the reach of the classical computational tools of fracture mechanics. Later, Bourdin et al. (2008) revisited Griffith's theory within the framework of the calculus of variations and developed its rigorous mathematical foundation supported by numerical examples.

1.5 **Nonlinear Fracture Mechanics**

Nonlinear fracture mechanics is also referred to as elasto-plastic fracture mechanics (EPFM). Elastic-plastic fracture mechanics deals with ductile fracture and is characterized by stable crack growth (ductile metals). The fracture process is accompanied by formation of a large plastic zone at the crack tip. The elastic crack tip stress reaches an infinite value, which occurs when the distance to the crack tip decreases to zero. Under this condition the material will reach the yield point before the crack tip is reached and the elastic solution is no longer valid. There are some inelastic deformations around the crack front that would make the assumption of linear elastic medium with infinite stresses at the crack tip highly unrealistic (Erdogan, 2000). For ductile materials such as steel, although equation (1.34) still holds, the surface energy, γ , predicted by Griffith's theory is usually unrealistically high. Irwin (1957) realized that plasticity must play a significant role in the fracture of ductile materials, as described in the next subsection.

When σ_{xx} reaches its maximum values, i.e. $\sigma_{xx} = \sigma_{max}$, the other two principal stresses can be written as $\sigma_2 = n\sigma_1$ and $\sigma_3 = m\sigma_1$. According to the Von Mises yield criterion, which assumes that yielding occurs when the specific distortional elastic energy W^a reaches a critical value W_c^d . The critical value is determined from a tensile test and expressed in terms of the yield stress σ_v and a function of the ratios n and m. The plastic constraint factor is equivalent to the ratio of the maximum principal stress at yield and the yield stress, i.e.

$$\frac{\sigma_{\text{max}}}{\sigma_y} = \frac{1}{\sqrt{1 - n - m + n^2 + m^2 m n}} \tag{1.35}$$

The requirement of σ_{yy} to be not larger than the yield stress, σ_{yy} results in loss of equilibrium in the crack plane ($\theta = 0$). Irwin (1958) developed a solution to this inconsistency, based on the enlargement of the plastic zone, such that the total y-force equals the force associated with the elastic solution.

1.5.1 Irwin's Modification

In ductile materials, a plastic zone may develop at the tip of the crack, as shown in Figure 1.8. As the applied load increases, the plastic zone increases in size until the crack grows and the material behind the crack tip unloads. The plastic loading and unloading cycle near the crack tip leads to the dissipation of energy in the form of heat. Hence, a dissipative term has to be added to the energy balance relation devised by Griffith for brittle materials. In physical terms, additional energy is needed for crack growth in ductile materials when compared to brittle materials. Irwin (1957, 1958) divided the energy into the stored elastic strain energy, which is released as a crack grows, and another portion due to the dissipated energy, which includes plastic dissipation and the surface energy. The dissipated energy provides the thermodynamic resistance to fracture, and its value per unit area of the crack $(G = -\partial U / \partial a)$ is

$$G = 2\gamma + G_n \tag{1.36}$$

where G_p is the plastic dissipation (and dissipation from other sources) per unit area of crack growth. The modified version of Griffith's energy criterion can then be written as

$$\sigma_f = \sqrt{\frac{EG}{\pi a}} \tag{1.37}$$

For brittle materials such as glass, the surface energy term dominates and $G \approx 2\gamma = 2 \text{ J/m}^2$. For ductile materials such as steel, the plastic dissipation term

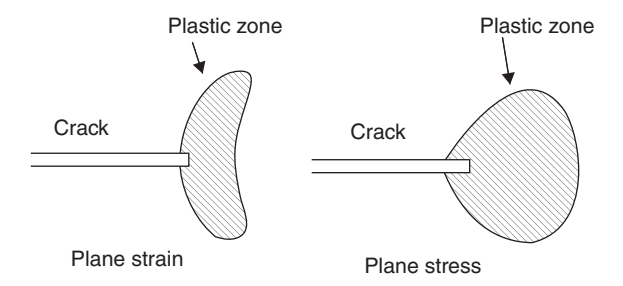


Figure 1.8 The plastic zone around a crack tip in a ductile material.

dominates and $G \approx G_p = 1000 \text{ J/m}^2$. For polymers close to the glass transition temperature the energy dissipation is in the range $G \approx 2 \text{ J/m}^2$ to 1000 J/m^2 . One basic assumption in Irwin's linear elastic fracture mechanics is that the size of the plastic zone is small compared to the crack length. However, this assumption is quite restrictive for certain types of failure in steel materials, which can be prone to brittle fracture and catastrophic failures.

Note that the crack extension occurs when $G = 2\gamma = R$, where R is called the material resistance to crack extension. Depending on how G and R vary with the crack size, the crack growth may be stable or unstable. A plot of R versus crack extension is called the crack growth resistance curve or R-curve. The corresponding plot of G versus crack extension is the driving force. This curve describes how the resistance to fracture increases with growing crack size in elastic-plastic materials. The R-curve is a plot of the total energy dissipation rate as a function of the crack size and can be used to examine the processes of slow stable crack growth and unstable fracture.

The condition for stable crack growth is $\frac{dG}{dR} \leq \frac{dR}{da}$, while the condition for unstable crack growth is $\frac{dG}{dR} > \frac{dR}{da}$. A material with a rising R-curve, however, cannot be uniquely

characterized by a single toughness value. According to the condition of unstable crack growth, a flaw structure fails when the driving force curve is tangential to the R-curve, but this point of tangency depends on the shape of the driving force, which depends on the configuration of the structure. The R-curve for an ideally brittle material is an invariant property. However, when nonlinear material behavior accompanies fracture, the R-curve can take a variety of shapes. Materials with rising R-curves can be characterized by the value of G at initiation of crack growth. This value, however, characterizes only the onset of crack growth and provides no information on the shape of the R-curve. Ideally, the R-curve, should only be a property of the material and should not depend on the size or shape of the crack body.

If the size of the plastic zone around a crack is small compared to the size of the crack, the energy required to grow the crack will not be critically dependent on the state of stress at the crack tip (Erdogan, 2000). In other words, a purely elastic solution may be used to calculate the amount of energy available for fracture. The energy release rate for crack growth or strain energy release rate may then be calculated as the change in elastic strain energy per unit area of crack growth, i.e.

$$G = -\left(\frac{\partial U}{\partial a}\right)_{p} = -\left(\frac{\partial U}{\partial a}\right)_{u} \tag{1.38}$$

where *U* is the elastic energy of the system. Subscripts *P* and *u* stand for fixed load and fixed displacement, respectively, while evaluating the above expressions.

For isotropic, homogeneous, and linear elastic material, Irwin showed that the strain energy release rate, G, for a mode-I crack (opening mode) is related to the stress intensity factor K_I :

$$G = G_I = \begin{cases} \frac{K_I^2}{E} & \text{plane stress} \\ \frac{(1 - v^2)K_I^2}{E} & \text{plain strain} \end{cases}$$
 (1.39a)

where ν is Poisson's ratio, and K_I is the stress intensity factor in mode-I. Irwin also showed that the strain energy release rate of a planar crack in a linear elastic body can be expressed in terms of the three modes' stress intensity factors for the most general loading conditions. For pure mode-II loading, relations (1.39a) are valid by replacing K_I by K_{II} . For mode-III loading, the strain energy release rate is given by the expression

$$G = K_{III}^2 \left(\frac{1}{2\bar{G}} \right) \tag{1.39b}$$

where \bar{G} is the shear modulus. Under general loading in plane strain, the strain energy release rate takes the following expression

$$G = \left(K_I^2 + K_{II}^2\right) \frac{\left(1 - v^2\right)}{E} + K_{III}^2 \frac{1}{2\bar{G}}$$
 (1.39c)

Irwin made an additional assumption that the size and shape of the energy dissipation zone remain approximately constant during brittle fracture. This assumption suggests that the energy needed to create a unit fracture surface is a constant and depends only on the material. This new material property was given the name fracture toughness and designated by G_{lc} . It is referred to as the critical stress intensity factor, K_c . For mode-I, fracture occurs when $K_I \ge K_{Ic}$. For the special case of plane strain deformation, K_c becomes K_{Ic} and is considered a material property. For mode-I, the critical value of the stress intensity, K_{lc} , is often used as an engineering design parameter in fracture mechanics. A statistical approach was introduced by Mull et al. (1987) to evaluate the cumulative probability of the critical energy release rate in composite structures. The analysis included the influence of fracture stress, critical crack length, and the angles of crack trajectory inclination, which were taken as random variables. The assessment of damage tolerance of aircraft attachment lugs was developed by Kathiresan et al. (1984). Solutions of stress distributions and stress intensity factors were obtained for various parameters. The parametric variations include lug outer-to-inner radius ratio corner and through-the-thickness cracks, crack lengths and aspect ratios, with and without interference-fit bushing and loads above and below yield of the lugs.

1.5.2 Crack Tip Element Method

The material fracture toughness and energy release rate are usually measured by a crack tip opening displacement test. The crack opening displacement (COD) method employs the crack tip opening displacement (CTOD), see Figure 1.9. Crack tip opening displacement (CTOD or δ) is defined as the displacement transverse to the crack tip, which is given by the hypotenuse of a 45°-45°-90° right triangle, as shown in Figure 1.9, The apparent advance of the crack tip is known as the crack opening stretch (COS). The CTOD test measures the resistance of a material to the propagation of a crack. CTOD is used for materials that can show some plastic deformation before failure occurs causing the tip to stretch open.

Fracture toughness is not a single-valued property, but it is a set of values that are functions of both the material and the fracture toughness. Experimental measurements of CTOD fracture toughness are supposed to be conducted on specimen thickness

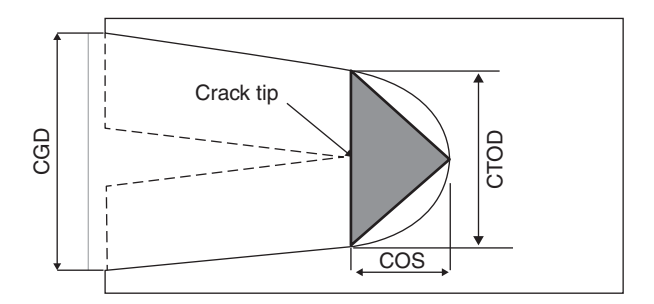


Figure 1.9 Definition of crack tip opening displacement (CTOD), crack opening stretch (COS), and clip gage displacement (CGD) or crack opening displacement (COD).

identical to the thickness of the structural element, as recommended by ASTM (1989a, 1989b, 2002) and BSI (1991). The CTOD is estimated from the measurement of the displacement of a clip gage across the crack tips. It is assumed that the CTOD, δ , is the sum of elastic δ_e and plastic, δ_p , components i.e. $\delta = \delta_e + \delta_p$. Approximate expressions for CTOD are given in Broek (1994) for LEFM and EPFM as

$$\delta_e \approx \frac{G}{\sigma_v} = \frac{K^2}{E\sigma_v}$$
 (LEFM)

$$\delta \approx \frac{J}{\sigma_y}$$
 (EPFM) (1.40b)

where G is the energy release rate (dU/da) and σ_v is the yield stress. Fracture occurs at a critical value of G (or K) or a critical value of the J-integral, as will be demonstrated later.

Paris-Erdogan Law

A power law relationship between the crack growth rate during cyclic loading was introduced by Paris and Erdogan (1963) together with the range of the stress intensity factor $\Delta K = K_{\text{max}} - K_{\text{min}}$, where K_{max} and K_{min} are the maximum and minimum stress intensity factors, respectively, in the form

$$\frac{da}{dN} = C\left(\Delta K\right)^m \tag{1.41}$$

where N is the number of load cycles, m is the slope between da/dN and ΔK (in log-log scale) as shown in Figure 1.10. C is the material constant and represents the coefficient at the interception of the log-log plot. The term on the left side, known as the crack growth rate, denotes the infinitesimal crack length growth per increasing number of load cycles. Figure 1.10 demonstrates three regions: region-I exhibits a slow crack growing, region-II represents the power-law region, and region-III is the terminal stage whose end defines the ultimate fracture.

The Paris law can be used to quantify the residual life (in terms of load cycles) of a specimen for a given crack size, defining the crack intensity factor as

$$K = \sigma Y \sqrt{\pi a} \tag{1.42}$$

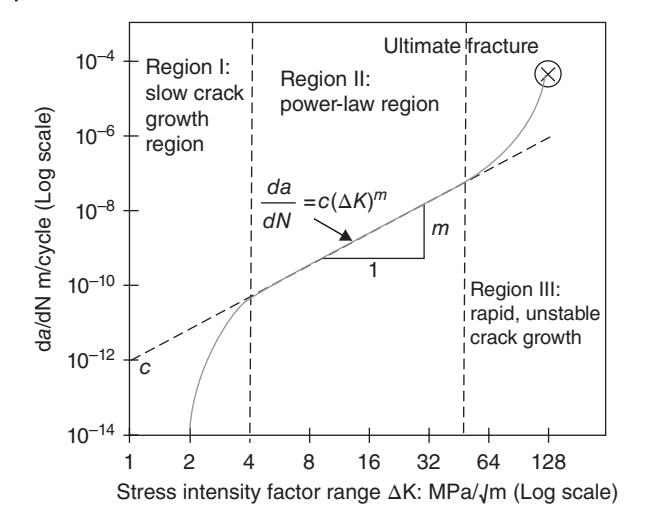


Figure 1.10 Typical relationship between the crack growth rate and the range of the stress intensity factor showing three regions of crack development for a given stress ratio.

where σ is a uniform tensile stress perpendicular to the crack plane and Y is a dimensionless parameter that depends on the geometry. The range of the stress intensity factor is

$$\Delta K = \Delta \sigma Y \sqrt{\pi a} \tag{1.43}$$

where $\Delta \sigma$ is the range of cyclic stress amplitude. Y=1 is taken for the case of a center crack in an infinite sheet. The remaining cycles can be found by substituting this equation in the Paris law

$$\frac{da}{dN} = C(\Delta K)^m = C(\Delta \sigma Y \sqrt{\pi a})^m \tag{1.44}$$

For relatively short cracks, *Y* can be assumed to be independent of *a*, and the differential equation can be solved using separation of variables to give

$$N_{f} = \frac{2\left(\frac{2-m}{a_{c}} - \frac{2-m}{a_{i}}\right)}{C(2-m)\left(\Delta\sigma Y \sqrt{\pi}\right)^{m}}$$
(1.45)

where N_f is the remaining number of cycles to fracture, a_c is the critical crack length above which instantaneous fracture will occur, and a_i is the initial crack length above which fatigue crack growth starts for the given stress range $\Delta \sigma$. If Y strongly depends on a, numerical methods might be required to find reasonable solutions.

Fatigue is the most significant failure mode in aircraft and ship structures, offshore platforms, bridges and road tankers. For example, Feng and Ren (2005) presented a design wave approach for fatigue assessment of ship structures. The fatigue assessment of a roll-on-roll-off (Ro/Ro) vessel was computed and the corresponding results were compared with the results from the simplified method and direct calculation method. Yoo et al. (2009) introduced a fatigue analysis model for typical structural parts.

Tian and Ji (2011) developed a model to analyze the low-cycle fatigue strength of ship structures. For aerospace structures, the most significant contribution was developed by the Air Force Grow Program known as AFGROW. A brief outline of AFGROW is given in the next section.

1.5.4 AFGROW Program

A damage tolerance analysis framework, that was developed by the Air Force Research Laboratory and known as AFGROW (Air Force Grow), was documented by Harter (1999). It allows users to analyze crack initiation, fatigue crack growth, and fracture in order to predict the life of metallic structures. The stress intensity factor library provides models for different crack geometries (including tension, bending, and bearing loading for many cases). An advanced multiple crack capability allows AFGROW to analyze two independent cracks in a plate (including hole effects), non-symmetric corner cracked. Finite element based solutions are available for two non-symmetric through cracks at holes as well as cracks growing toward holes. This capability allows AFGROW to handle cases with more than one crack growing from a row of fastener holes. AFGROW implements five different material models to determine crack growth per applied cyclic loading.

1) The Walker equation (Walker, 1970) is essentially an enhancement of the Paris equation that includes a means of accounting for the effect of stress ratio (minimum stress/maximum stress, i.e. $\bar{\sigma} = \sigma_{\min} / \sigma_{\max}$) on crack growth rate. This equation takes the form

$$\frac{da}{dN} = C \left[\Delta K \left(1 - \overline{\sigma} \right)^{(m-1)} \right]^n; \quad \text{for} \quad \overline{\sigma} \ge 0$$
 (1.46a)

$$\frac{da}{dN} = C \left[K_{\text{max}} \left(1 - \overline{\sigma} \right)^{(1-m)} \right]^n; \quad \text{for} \quad \overline{\sigma} < 0$$
 (1.46b)

Harter (1999) highlighted the reasons for using a different form of the Walker equation when $\bar{\sigma}$ < 0. The first is that it is more convenient to use K_{max} in place of ΔK for negative values of stress ratio, $\bar{\sigma}$. If ΔK were used for negative $\bar{\sigma}$ values, the crack growth rate curves would continue to shift to the right as $\bar{\sigma}$ decreases and eventually converge to a factor $(1-\overline{\sigma})$ of ΔK at $\overline{\sigma} = 0$. The second reason is that the shift in crack growth rate is controlled by the term $(1-\bar{\sigma})^{(m-1)}$ when $\bar{\sigma} \ge 0$ for which $(1-\bar{\sigma})$ would be less than 1 and thus as m increases, the shift decreases. Generally, m is limited within the range [0,1).

2) The Forman equation (Forman et al., 1967) is an improvement of the Walker equation and includes a means to account for the upper portion of the $da/dN - \Delta K$ curve where the data becomes asymptotic to the value of ΔK at fracture. The Forman equation used in AFGROW is

$$\frac{da}{dN} = \frac{C\Delta K^n}{\left[\left(1 - \bar{\sigma} \right) K_c - \Delta K \right]} \tag{1.47}$$

The Forman equation is not flexible in modeling data shifting as a function of stress ratio, $\bar{\sigma}$. There is no parameter to adjust the $\bar{\sigma}$ shift directly. The amount of shifting is controlled by the plane stress fracture toughness of a given material.

- 3) Harter T-method (Harter, 1994) replaced the original name "point-by-point Walker shift method." Harter first developed the method as a means of interpolating and/ or extrapolating crack growth rate data using a limited amount of tabular crack growth rate test data. The data shifting is handled by using K_{max} in place of ΔK when $\bar{\sigma}$ < 0, and the shifting data is handled by using Walker equation (1.43a). At a given da/dN, the relationship reduces to $\Delta K = \Delta K_{\bar{\sigma}=0} (1-\bar{\sigma})^{(1-m)}$, for $\bar{\sigma} \ge 0.0$, and $K_{\text{max}} = \Delta K_{\overline{\sigma}=0} (1 - \overline{\sigma})^{(m-1)}$, for $\overline{\sigma} < 0.0$. This method is simply a way to interpolate/ extrapolate data in log-log scale by using the exponential form.
- 4) The NASGRO equation (Forman and Mettu, 1992) was used in NASA's crack growth life prediction program, NASGRO, Version 3.0. Few additional parameters in the NASGRO equation were introduced by AFGROW (explained later in this section). Forman and Mettu (1992), Newman (1992), and others at NLR and ESA developed the elements of the NASGRO crack growth rate equation:

$$\frac{da}{dN} = C \left[\left(\frac{1 - f}{1 - \bar{\sigma}} \right) \Delta K \right]^{n} \frac{\left(1 - \frac{\Delta K_{th}}{\Delta K} \right)^{p}}{\left(1 - \frac{K_{\text{max}}}{K_{crit}} \right)^{q}}$$
(1.48)

where C, n, p, and q are empirical constants, α is the plane stress/strain constant factor, and $\sigma_{\rm max}/\sigma_0$ is the ratio of the maximum applied stress to the flow stress, $A_0 = (0.825 - 34\alpha + 0.5\alpha 2)[\cos(\pi S_{\text{max}} / 2\sigma_0)]^{1/\alpha}$, $A_1 = (0.415 - 0.071\alpha)\frac{\sigma_{\text{max}}}{\sigma_0}$, $A_2 = 1 - A_0 - A_1 - A_3 A_3 = 2A_0 + A_1 - 1$, and

$$f = \frac{K_{op}}{K_{\max}} = \begin{cases} \max \left(R, A_0 + A_1 \overline{\sigma} + A_2 \overline{\sigma}^2 + A_3 \overline{\sigma}^3 \right) & \overline{\sigma} \ge 0 \\ A_0 + A_1 \overline{\sigma} & -2 \le \overline{\sigma} < 0. \\ A_0 - 2A_1 & \overline{\sigma} < -2 \end{cases}$$

5) A tabular lookup crack growth rate capability is provided in AFGROW to allow users to input their own crack growth rate curves. The tabular data utilizes the Walker equation on a point-by-point basis (Harter T-method) to extrapolate/interpolate data for any value of the stress ratio $\bar{\sigma}$. The difference in the tabular lookup method is that the user doesn't have to calculate all of the m values (AFGROW does it internally between each possible pair of input $\bar{\sigma}$ curves).

Energy Release Integrals

Most engineering materials show some nonlinear elastic and inelastic behavior under operating conditions involving large loads. In such materials the plastic zone at a crack tip may have a size of the same order of magnitude as the crack size. Furthermore, the size and shape of the plastic zone may change as the applied load increases and also as the crack length increases. Thus a nonlinear fracture theory is needed for elastic-plastic materials that can account for the local conditions for initial crack growth such as the nucleation, growth, and coalescence of voids, or decohesion at a crack tip.

Numerical algorithms such as the finite element and boundary element methods have been used for estimating the stress intensity factors. These methods have been classified in local or global methods (Ortiz et al., 2006). The local methods employ the local variables defined near the crack tip, whereas the global ones are based on the far field variables or variables associated to the entire domain. The global methods are based on conservation integrals such as J-, M-, L-, and H-integrals. These integrals constitute a more robust approach since they eliminate the need to solve local singular stress fields very accurately. The next subsections outline the main features of J-, M-, L- and *H*-integrals.

The stress intensity factors in mixed-mode cracks can be obtained using J-integral. In this case, it is necessary to decouple the stress and strain fields into the symmetric mode-I and both anti-symmetric mode-II and mode-III (Huber et al., 1993; Rigby and Aliabadi, 1993). The interaction integral (M-integral) is based on the superposition of the two equilibrium states and was originally formulated by Knowles and Sternberg (1978). The two-state L-integral was employed by Choi and Earmme (1992) to compute stress intensity factors for circular arc-shape cracks. The H-integral is the conjugate integral due to Büeckner (1973). The H-integral is derived from the well-known second Betti reciprocal theorem. It was applied for estimating the stress intensity factor at two-dimensional corners in isotropic, anisotropic, and dissimilar materials by Sinclair et al. (1984) and Carpenter (1984, 1995). For three-dimensional crack problems a pathindependent expression was derived by Meda et al. (1998), starting from the H-integral. All of these methodologies based on path-independent integrals necessarily require the use of an auxiliary field. The fact that the H-integral computation requires only evaluation of natural variables like displacements and stresses represents an inherent advantage of this approach, which can imply its better accuracy in comparison with other conservation integrals that require gradients of displacements and/or stresses.

1.5.5.1 J-Integral

Elastic-plastic fracture mechanics applies to materials that exhibit time-independent, nonlinear behavior (plastic deformation). There are two-parameters characterizing the nonlinear behavior at the crack tip, namely the crack tip opening displacement (CTOD) and the *J*-integral. The *J*-integral describes the strain energy release rate, -dU/da, or energy per unit fracture surface area in a body subjected to monotonic loading. This is true, under quasi-static conditions, both for linear elastic materials and for materials that experience small-scale yielding at the crack tip. It may be regarded as a change of potential energy of the structure with an increment of crack extension. Rice (1968) also showed that the value of the *J*-integral represents the energy release rate for planar crack growth. With reference to Figure 1.11, the *J*-integral is a line integral given by the expression

$$J = \int_{\Gamma} \left(W(x, y) dy - \vec{T} \cdot \frac{\partial \vec{u}}{\partial x} ds \right)$$
 (1.49)

where $W(x,y) = \int_{0}^{\varepsilon_{ij}} \sigma_{ij} \cdot d(\varepsilon_{ij})$ is the strain energy density, $\vec{T} = \vec{n} \cdot \vec{\sigma}$ is the surface traction vector acting on a segment ds, $\vec{\sigma}$ is the Cauchy stress tensor, \vec{n} is the normal to the curve Γ , and \vec{u} is a displacement vector along arc s.

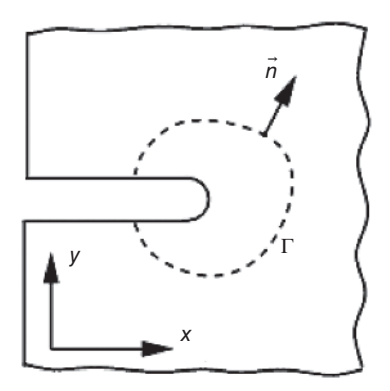


Figure 1.11 *J*-integral around a crack tip in two dimensions.

Integral (1.49) is taken as a toughness measure to describe the case where there is sufficient crack tip deformation such that the part no longer obeys the linear-elastic approximation. It was independently developed by Cherepanov (1967) and Rice (1968). It was shown that an energetic contour path integral is independent of the path around a crack. It assumes nonlinear elastic deformation ahead of the crack tip. This analysis is limited to situations where plastic deformation at the crack tip does not extend to the furthest edge of the loaded part.

For plane strain, under mode-I loading, this relation takes the form:

$$J_{Ic} = G_{Ic} = K_{Ic}^2 \left(\frac{1 - v^2}{E}\right) \tag{1.50}$$

where G_{Ic} is the critical strain energy release rate, K_{Ic} is the fracture toughness in mode-I loading. For mode-II and mode-III loadings, the relation between the *J*-integral and the mode fracture toughness takes the same form after replacing the subscript I by II or III, respectively.

An early survey of the analysis of crack tip stress and strain fields for stationary and growing cracks in inelastic solids under monotonic loading was presented by Hutchinson (1982). The *J*-integral was defined as a measure of the singularity field from the small strain deformation theory of plasticity. This description of an elastic-plastic material breaks down sufficiently near the tip due to effects not modeled by deformation theory such as strongly non-proportional plastic deformations, finite strain effects, or microvoiding and cracking. Any appreciable increases in the *J*-integral above the value at which crack growth starts are possible with only small amounts of accompanying crack advance. Under these circumstances, the importance of the initiation of crack growth becomes secondary to the point at which a small amount of crack advance becomes unstable. It was indicated by Hutchinson (1982) that the *J*-resistance curve approach may be an important range of applications, fairly severe restrictions on its use may be invoked, including limitations to small amounts of crack growth.

Consider a stain hardening material for which the nonlinear (plastic) part of the strain, ε , is given in terms of the uniaxial stress, σ , by the power law (Ramberg and Osgood, 1943):

$$\frac{\varepsilon}{\varepsilon_0} = \frac{\sigma}{\sigma_y} + \alpha \left(\frac{\sigma}{\sigma_y}\right)^n \approx \alpha \left(\frac{\sigma}{\sigma_y}\right)^n, \quad \text{for } \varepsilon >> \varepsilon_0$$
 (1.51)

where σ_y is the yield stress, $\varepsilon_0 = \sigma_y/E$, and E is Young's modulus. In this case, the singularity field defined by Hutchinson (1968a, 1968b) and Rice and Rosengren (1968) is given by the expressions

$$\sigma_{ij} \approx \sigma_{y} \left(\frac{J}{\alpha \sigma_{y} \varepsilon_{0} I_{n} r} \right)^{\frac{1}{n+1}} \tilde{\sigma}_{ij} \left(\theta, n \right), \quad \varepsilon_{ij} \approx \alpha \varepsilon_{0} \left(\frac{J}{\alpha \sigma_{y} \varepsilon_{0} I_{n} r} \right)^{\frac{n}{n+1}} \tilde{\varepsilon}_{ij} \left(\theta, n \right)$$

$$u_{i} - u_{i}^{0} \approx \alpha \varepsilon_{0} r \left(\frac{J}{\alpha \sigma_{y} \varepsilon_{0} I_{n} r} \right)^{\frac{n}{n+1}} \tilde{u}_{i} \left(\theta, n \right)$$

$$(1.52a,b,c)$$

where r and θ are planar-polar coordinates centered at the tip with θ measured from the line ahead of the crack, as shown in Figure 1.5. The dimensionless θ -variations, $\tilde{\sigma}_{ij}$, $\tilde{\varepsilon}_{ij}$, and \tilde{u}_i depend on the symmetry of the field and whether plane strain or plane stress holds as the tip is approached, as does the normalizing constant I_n . For a hardening material with n finite, equations (1.52a) and (1.52b) imply a unique relation between the stress and strain fields sufficiently near the tip. If r_0 represents the radius of the region at the tip within the singular field, as given by equations (1.52a) and (1.52b), then it measures the zone of dominance of the singular field.

Near the crack tip, it is essential that the region of incipient material separation and the region over which finite strain effects become important be contained within the zone of dominance measured by the radius r_0 . In most ductile metals the fracture process zone is roughly the same size as the finite strain region near the blunted tip of the crack. Finite element solutions for plane strain mode-I, in small scale, developed by McMeeking (1977), showed that finite strain effects are only important within a radius of about 2–3 times the crack tip opening displacement, δ_t . Outside this radius there is little difference between the predictions of small strain theory and finite strain theory. For mode-I in-plane strain the zone of dominance of the J-fields must satisfy the condition

$$r_0 > 3\delta_t \tag{1.53}$$

provided that the *J*-integral is to be unique measure of crack tip behavior under mono-

Other configurations include the center-cracked strip in plane strain tension, which lose the high triaxial state of stress ahead of the crack tip under fully plastic yielding. Accordingly, the near-tip fracture environment cannot be correlated with cases of triaxial. The zone of the singularity field (Hutchinson, 1968a, 1968b; Rice and Rosengren, 1968) of dominance radius r_0 approaches zero with zero strain hardening $(n \to \infty)$ for the fully plastic center-cracked strip under tension. The zone of dominance radius r_0 according to Hutchinson (1968a, 1968b) and Rice and Rosengren (1968) the field goes to zero with zero strain hardening $(n \rightarrow \infty)$ for the fully plastic center-cracked strip under tension. Even in the presence of moderate strain hardening, the radius r_0 will tend to be very small. Numerical studies of the fully yielded center-cracked strip by

McMeeking and Parks (1979) and Shih and German (1981) indicated that $R \approx 0.01b$ where b is the uncracked ligament length, and

$$b > 200 \frac{J}{\sigma_0}$$
 for $n = 10$ (1.54)

McMeeking and Rice (1975) presented an Eulerian finite element formulation for problems of large elastic-plastic flow. The method is based on Hill's variational principle for incremental deformations, and is convenient to isotropically hardening Prandtl-Reuss materials. The formulation was presented in a form convenient for finite element programs, for "small strain" elastic-plastic analysis, to be simply and rigorously adapted to problems involving arbitrary amounts of deformation and arbitrary levels of stress. Finite-strain/finite-element analyses of deeply cracked plane-strain center-notch panel and single-edge crack bend specimens were developed by McMeeking and Parks (1979) who employed non-hardening and powerlaw-hardening constitutive laws. The deformation was obtained from small-scale yielding into the fully plastic range. The *J*-integral can be obtained experimentally by analyzing an edge cracked plate in bending, assuming the plastic region spreads over the total ligament length.

1.5.5.2 M-Integral (Interaction Integral)

The M-integral is another measure of energy release rate, which can be interpreted as the energy release rate associated with self-similar expansion within a crack tip bounding contour (Short, 1987). The M-integral concept was earlier developed by Eshelby (1956, 1970, 1975), Knowles and Sternberg (1972), Budiansky and Rice (1973), Freund (1978), Herrmann and Herrmann (1981), and King and Herrmann (1981). The two-dimensional mixed-mode crack problem was reduced to the determination of mixed-mode stress-intensity factor solutions in terms of conservation integrals involving known auxiliary solutions. Yau et al. (1980) developed the M-integral from the J-integral as a way to extract the stress intensity factors for the three fracture modes from the global energy release rate. The actual field constitutes $(\sigma_{ij}^{(1)}, \varepsilon_{ij}^{(1)}, u_i^{(1)})$ while the auxiliary field is denoted by $\left(\sigma_{ij}^{(2)}, \varepsilon_{ij}^{(2)}, u_i^{(2)}\right)$. To obtain the *M*-integral for linear elastic materials, two solutions were assumed and superposed:

$$\sigma_{ij} = \sigma_{ij}^{(1)} + \sigma_{ij}^{(2)}, \ \varepsilon_{ij} = \varepsilon_{ij}^{(1)} + \varepsilon_{ij}^{(2)}, \ u_i = u_i^{(1)} + u_i^{(2)}, K_i = K_i^{(1)} + K_i^{(2)}$$
(1.55)

The formulation of M-integral due to Song and Paulino (2006) is based on assuming that the crack faces are traction-free. They introduced a weight function q, which assumes the value 1 at the stress intensity evaluation point and zero on the outer boundary of the domain of integration Γ as shown in Figure 1.12. The q function can be regarded of as a virtual crack extension. The generalized *J*-integral takes the form

$$J = \lim_{\Gamma_s \to 0} \int_{\Gamma_s} \left(W \delta_{1j} - \sigma_{ij} u_{i,1} \right) n_j d\Gamma = \lim_{\Gamma_s \to 0} \int_{\Gamma} \left(W \delta_{1j} - \sigma_{ij} u_{i,1} \right) m_j q d\Gamma$$
(1.56)

where *W* is the strain energy density, the contour of integration $\Gamma = \Gamma_0 + \Gamma^+ - \Gamma_s + \Gamma^$ is as shown in Figure 1.13, and δ is the Kronecker delta, i.e. $\delta_{ij} = 1$ if i = j, otherwise

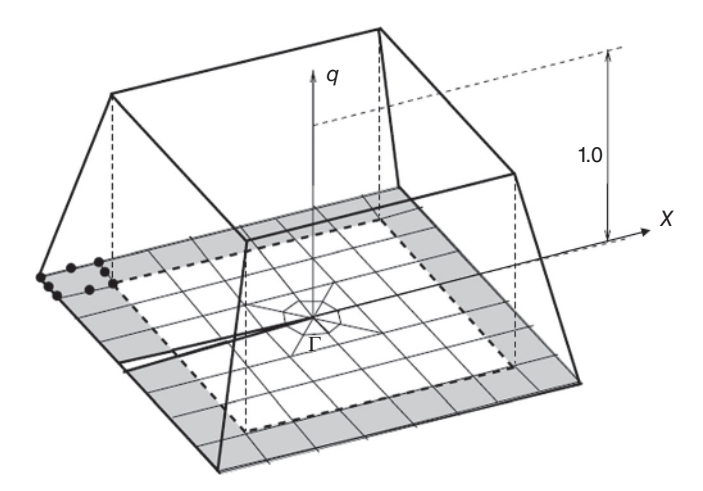


Figure 1.12 Concept of the weighting *q*-function. (Adapted from Song and Paulino, 2006)

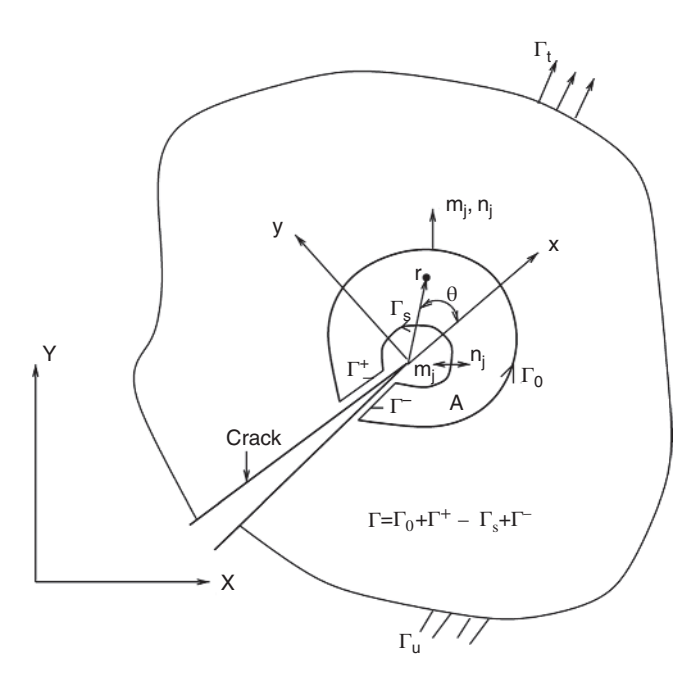


Figure 1.13 Contours near the crack tip showing the normal vectors $m_j = n_j$ for Γ_0 , Γ^+ and Γ^- ; and $m_j = -n_j$ on Γ_s used in the transformation from line integral to equivalent domain integral. (Song and Paulino, 2006)

it is zero. Applying the divergence theorem, equation (1.56) can be transformed into the equivalent domain integral

$$J = \int_{A} (\sigma_{ij} u_{i,1} - W \delta_{1j}) q_{,j} dA + \int_{A} (\sigma_{ij} u_{i,1} - W \delta_{1j})_{,j} q dA$$
 (1.57)

where ",j" denotes the gradient with respect to x_j , $W_{,1} = \frac{1}{2}\sigma_{ij,1}\varepsilon_{ij} + \frac{1}{2}\sigma_{ij}\varepsilon_{ij,1}$, and $(\sigma_{ij}u_{i,1})_j = \sigma_{ij,j}u_{i,1} + \sigma_{ij}u_{i,1j}$. Introducing these expressions into equation (1.57) gives

$$J = \int_{A} \left(\sigma_{ij} u_{i,1} - W \delta_{1j} \right) q_{,j} dA + \int_{A} \left(\sigma_{ij,j} u_{i,1} + \sigma_{ij} u_{i,1j} - \frac{1}{2} \sigma_{ij,1} \varepsilon_{ij} - \frac{1}{2} \sigma_{ij} \varepsilon_{ij,1} \right) q dA \quad (1.58)$$

The interaction integral utilizes two admissible fields, namely auxiliary and actual fields. The auxiliary field is based on known fields such as Williams' solution (1957), while actual field utilizes displacements, strains, and stresses obtained by means of numerical methods. The *J*-integral of the two states is

$$\begin{split} J &= \int_{A} \left\{ \left(\sigma_{ij}^{(2)} + \sigma_{ij}^{(1)} \right) \left(u_{i,1}^{(2)} + u_{i,1}^{(1)} \right) - \frac{1}{2} \left(\sigma_{ik}^{(2)} + \sigma_{ik}^{(1)} \right) \left(\varepsilon_{ik}^{(2)} + \varepsilon_{ik}^{(1)} \right) \delta_{1j} \right\} q_{,j} dA \\ &+ \int_{A} \left\{ \left(\sigma_{ij,j}^{(2)} + \sigma_{ij,j}^{(1)} \right) \left(u_{i,1}^{(2)} + u_{i,1}^{(1)} \right) + \left(\sigma_{ij}^{(2)} + \sigma_{ij}^{(1)} \right) \left(u_{i,1j}^{(2)} + u_{i,1j}^{(1)} \right) \right\} q dA \\ &- \frac{1}{2} \int_{A} \left\{ \left(\sigma_{ij,1}^{(2)} + \sigma_{ij,1}^{(1)} \right) \left(\varepsilon_{ij}^{(2)} + \varepsilon_{ij}^{(1)} \right) + \left(\sigma_{ij}^{(2)} + \sigma_{ij}^{(1)} \right) \left(\varepsilon_{ij,1}^{(2)} + \varepsilon_{ij,1}^{(1)} \right) \right\} q dA \\ &= J^{(1)} + J^{(2)} + M \end{split} \tag{1.59}$$

where

$$J^{(1)} = \int_{A} \left(\sigma_{ij}^{(1)} u_{i,1}^{(1)} - \frac{1}{2} \sigma_{ik}^{(1)} \varepsilon_{ik}^{(1)} \delta_{1j} \right) q_{,j} dA + \int_{A} \left(\sigma_{ij,j}^{(1)} u_{i,1}^{(1)} + \sigma_{ij}^{(1)} u_{i,1j}^{(1)} - \frac{1}{2} \sigma_{ij,1}^{(1)} \varepsilon_{ij}^{(1)} - \frac{1}{2} \sigma_{ij}^{(1)} \varepsilon_{ij,1}^{(1)} \right) q dA$$

$$(1.60a)$$

$$J^{(2)} = \int_{A} \left(\sigma_{ij}^{(2)} u_{i,1}^{(2)} - \frac{1}{2} \sigma_{ik}^{(2)} \varepsilon_{ik}^{(2)} \delta_{1j} \right) q_{,j} dA + \int_{A} \left(\sigma_{ij,j}^{(2)} u_{i,1}^{(2)} + \sigma_{ij}^{(2)} u_{i,1j}^{(2)} - \frac{1}{2} \sigma_{ij,1}^{(2)} \varepsilon_{ij}^{(2)} - \frac{1}{2} \sigma_{ij}^{(2)} \varepsilon_{ij,1}^{(2)} \right) q dA$$

$$\tag{1.60b}$$

$$M = \int_{A} \left\{ \left(\sigma_{ij}^{(2)} u_{i,1}^{(1)} + \sigma_{ij}^{(1)} u_{i,1}^{(2)} \right) - \frac{1}{2} \left(\sigma_{ik}^{(2)} \varepsilon_{ik}^{(1)} + \sigma_{ik}^{(1)} \varepsilon_{ik}^{(2)} \right) \delta_{1j} \right\} q_{,j} dA$$

$$+ \int_{A} \left\{ \left(\sigma_{ij,j}^{(2)} u_{i,1}^{(1)} + \sigma_{ij,j}^{(1)} u_{i,1}^{(2)} \right) + \left(\sigma_{ij}^{(2)} u_{i,1j}^{(1)} + \sigma_{ij}^{(1)} u_{i,1j}^{(2)} \right) \right\} q dA$$

$$- \frac{1}{2} \int_{A} \left\{ \left(\sigma_{ij,1}^{(2)} \varepsilon_{ij}^{(1)} + \sigma_{ij,1}^{(1)} \varepsilon_{ij}^{(2)} \right) + \left(\sigma_{ij}^{(2)} \varepsilon_{ij,1}^{(1)} + \sigma_{ij}^{(1)} \varepsilon_{ij,1}^{(2)} \right) \right\} q dA$$

$$(1.60c)$$

The above formulation was obtained for the equilibrium state under stationary condition. The relationship between stress intensity factor and J-integral for general mixed-mode problems in two-dimensions near the crack tip (region surrounded by Γ_s) may be written in the form:

$$J_{\text{local}} = \frac{K_I^2}{E_{\text{tip}}^*} + \frac{K_{II}^2}{E_{\text{tip}}^*}$$
 (1.61)

where E^* is defined as

$$E_{\text{tip}}^{*} = \begin{cases} E & \text{for plane stress} \\ \frac{E}{1 - v^{2}} & \text{for plane strain} \end{cases}$$
 (1.62)

For the superimposed fields of actual and auxiliary fields, the relationship between J-integral and stress intensity factors of actual and auxiliary field is obtained in the form

$$J_{\text{local}}^{s} = \frac{1}{E_{\text{tip}}^{*}} \left[\left(K_{I}^{(1)} + K_{I}^{(2)} \right)^{2} + \left(K_{II}^{(1)} + K_{II}^{(2)} \right)^{2} \right] = J_{\text{local}}^{(1)} + J_{\text{local}}^{(2)} + M_{\text{local}}$$
(1.63)

where

$$M_{\text{local}} = \frac{2}{E_{\text{tip}}^*} \left(K_I^{(1)} K_I^{(2)} + K_{II}^{(1)} K_{II}^{(2)} \right) \tag{1.64}$$

For a particular choice of auxiliary mode-I and mode-II stress intensity factors of actual fields, the stress intensity factors of the actual field are decoupled and were obtained by Yau et al. (1980), Song and Paulino (2006), and Liang et al. (2010) in the form

$$K_I^{(1)} = \frac{E_{\text{tip}}^*}{2} M_{\text{local}}, \text{ with } K_I^{(2)} = 1, \text{ and } K_{II}^{(2)} = 0$$
 (1.65a)

$$K_{II}^{(1)} = \frac{E_{\text{tip}}^*}{2} M_{\text{local}}, \text{ with } K_{I}^{(2)} = 0, \text{ and } K_{II}^{(2)} = 1$$
 (1.65b)

A similar technique can be used to formulate a three-dimensional equivalent domain version of the M-integral, where the integration takes place over a volume (e.g. Wawrzynek et al., 2005).

For calculating the stress intensity factors associated with piezoelectric material for an impermeable crack, Banks-Sills et al. (2008) derived a conservative integral as an extension of the M-integral or interaction energy integral for mode separation. The method of displacement extrapolation was extended to validate the results obtained with the conservative integral. An M-integral describing the mixed-mode during a creep crack growth process in viscoelastic orthotropic media was developed by Mouton Pitti et al. (2008), based on an energetic approach using conservative laws. The fracture algorithm is implemented in finite element software and coupled with an incremental viscoelastic formulation and an automatic crack growth simulation. This integral provides the computation of stress intensity factors and energy release rate for each fracture mode. The coupling between the M-integral and an incremental viscoelastic formulation was implemented in finite element software and introduced in an automatic crack growth algorithm, considering the crack lip un-cohesion and the crack tip vicinity in a process zone. A numerical validation, in terms of energy release rate and stress intensity factors, was performed on a compact-tension-shear specimen under mixed-mode loading for different crack growth speeds.

The M-integral concept was extended by Hu and Chen (2009) to study the degradation of a brittle plane strip caused by irreversible evolution in which the cracks coalesce under monotonically increasing loading. The change of the M-integral before and after coalescence of two neighboring cracks inclined to each other was monitored. Finite element analyses revealed that different orientations of the two cracks led to different critical values of the M-integral at which the coalescence occurs. It was concluded that the M-integral does play an important role in the description of the damage extent and damage evolution. It was found that there is an inherent relation between the M-integral and the reduction of the effective elastic moduli as the orientation of one crack varies, i.e. the larger the M-integral, the larger the reduction. Furthermore, the M-integral was found to be inherently related to the change of the total potential energy for a damaged brittle material regardless of the detailed damage features or damage evolution. Liang et al. (2010) applied the M-integral to calculating stress intensity factor by calculating the stress field and displacement field near to the crack tip, according to the extended finite element method.

1.5.5.3 L-Integral

The *L*-integral is related to the energy release rate due to a virtual rotation. The *L*-integral plays an important role in describing the damage content, the damage evolution, and the final failure, especially in the cases where the microvoids are not distributed symmetrically (Hermann and Hermann, 1983). Only when the damage induced from microvoids is symmetrically distributed does the *M*-integral play a dominant role without any treatment of the *L*-integral. To obtain the *L*-integral the invariant curl operator was used, while for the *M*-integral the divergence operator was employed.

In the two-dimensional infinitesimal deformation, the L-integral was defined by Knowles and Sternberg (1972) in the form

$$L = \oint \varepsilon_{3ij} \left(w X_j n_i + T_i u_j - T_k \frac{\partial u_k}{\partial X_i} X_j \right) ds$$
 (1.66a)

where w is the strain energy density, T_i is the traction vector, u_i is the displacement, n_i is the unit outward normal vector, X_i are the plane coordinate axes, and ε_{3i} is the twodimensional alternator. Park and Earmme (1986) showed that the L-integral satisfies the conservation law, i.e. L = 0 in a composite body composed of two homogeneous isotropic elastic bodies with a circular interface. They also showed that the integral is a path-independent. It is related to the J-integral for a circular arc-shaped interfacial crack, and thus can be written in terms of mixed-mode stress intensity factors, i.e. Choi and Earmme (1992)

$$L = \int_{\Gamma} \varepsilon_{3ij} \left(wX_j n_i + T_i u_j - T_k \frac{\partial u_k}{\partial X_i} X_j \right) ds = -RJ_t = -Rh \left(K_I^2 + K_{II}^2 \right)$$
 (1.66b)

where Γ is the contour enclosing the crack tip with end points on the crack faces, R is the radius of the circular arc crack, J_t the J-integral defined in the local coordinate system (x_1, x_2) whose origin is located at the crack tip, and $h = \frac{1}{15} \left(\frac{1 + \kappa_1}{\mu_1} + \frac{1 + \kappa_2}{\mu_2} \right)$, $\kappa_j = 3 - 4\nu_j$ for plane strain, or $\kappa_j = \frac{3 - \nu_j}{1 + \nu_j}$ for plane stress, and μ_j and ν_j (j = 1, 2) are the shear modulus and Poisson's ratio, respectively.

The property of the *M*-integral being rather different in two- and three-dimensions now becomes the most transparent. The relationship between M- and L-integrals was developed by Chen, Y.H. (2002) in the form, $L = -\frac{1}{2} \frac{\partial M}{\partial \theta}$, where θ is the rotation angle for a center crack in an infinite elastic body under remote uniform loading.

1.5.5.4 H-Integral

The path-independent integral for a two-dimensional crack referred to as the H-integral was originally developed by Büeckner (1973). In terms of the actual and auxiliary and elastic fields, the *H*-integral may be expressed in the form (Ortiz et al., 2006)

$$H = \int_{\Gamma} \left(T_i^{(1)} u_i^{(2)} - T_i^{(2)} u_i^{(1)} \right) d\Gamma \tag{1.67}$$

where T_i is the traction vector and Γ is an arbitrary path around the corner tip. Note that H = 0 when actual and auxiliary elastic solutions have a finite energy in the corner tip neighborhood. The asymptotic series expansion of the displacement field (Aksentian, 1967; Hartranft and Sih, 1969; Andersson et al., 1995) at the neighborhood was expressed in terms of the angular eigen-functions and associated stress intensity factors. Based on the property of bi-orthogonality between the families of the eigenfunctions associated to positive and negative eigenvalues, Ortiz et al. (2006) showed that the H-integral given by equation (1.67) is proportional to the stress intensity functions of the actual field, i.e.

$$K_{mp} = \int_{\Gamma} \left(T_i^{(1)} u_i^{(2)} - T_i^{(2)} u_i^{(1)} \right) d\Gamma \tag{1.68}$$

where an adequate normalization factor for the auxiliary field was chosen. A domainindependent integral formulation for numerical computation of stress intensity factors along crack fronts and edges in three-dimensional problems was proposed by Ortiz et al. (2006). The formulation was implemented as a post-processing module in a boundary element method code.

Note that both LEFM and EPFM outlined in the previous sections deal with metallic structures. However, for the case of composite and sandwich structures the treatment will involve singularities due to the edge effects, which are referred to as the boundarylayer effects. These effects will be discussed in Section 1.6.

1.5.6 Mechanisms of Crack Propagation

There are different mechanisms in the way a crack propagates through the material, depending on the material type and its geometry, plus loading and environmental conditions. Schreurs (2011) identified these mechanisms as shear fracture, cleavage fracture, fatigue fracture, crazing, and de-adhesion. This subsection will address four main mechanisms in fracture mechanics.

1.5.6.1 Fatigue Fracture

Under cyclic loading, the crack tip will travel a very short distance in each loading cycle, provided that the stress is high enough, but not too high to cause sudden global fracture. This mechanism is referred to as fatigue. Because crack propagation is very small in each individual load cycle, a large number of cycles is needed before total failure occurs. The number of cycles to failure N_f is strongly related to the stress amplitude $\Delta \sigma = (\sigma_{\text{max}} - \sigma_{\text{min}})/2$ and the average stress $<\sigma>=(\sigma_{\text{max}} + \sigma_{\text{min}})/2$.

The mechanisms of fatigue-crack propagation were examined with particular emphasis on the similarities and differences between cyclic crack growth in ductile materials, such as metals, and corresponding behavior in brittle materials, such as intermetallics and ceramics (Ritchie, 1999). The process of fatigue crack growth was considered as a mutual competition between *intrinsic* mechanisms of crack advance ahead of the crack tip (e.g. alternating crack tip blunting and re-sharpening), which promote crack growth, and *extrinsic* mechanisms of crack tip shielding behind the tip (e.g. crack closure and bridging), which impede it (Gilbert et al., 1999). The mechanisms associated with fatigue-crack propagation in brittle materials, such as monolithic and composite ceramics and intermetallics, were found to be quite distinct from those commonly encountered in metal fatigue; moreover, their crack-growth rate (da/dN) behavior displays a markedly higher sensitivity to the applied stress intensity (K) than is observed in most metals (Ritchie and Dauskardt, 1991). As indicated by Ritchie (1988), crack growth is promoted *ahead* of the crack tip by *intrinsic* microstructural damage mechanisms, and impeded by *extrinsic* mechanisms acting primarily *behind* the crack tip, which serve to 'shield' the crack tip from the far-field driving forces.

1.5.6.2 Shear Fracture

When a crystalline material is loaded, dislocations will start to move through the lattice due to local shear stresses. Also, the number of dislocations will increase. Because the internal structure is changed irreversibly, the macroscopic deformation is permanent (plastic). The dislocations will coalesce at grain boundaries and accumulate to make a void, which may grow until it is transformed into a macroscopic crack. One or more cracks may then grow and lead to failure. Because the origin and growth of cracks is provoked by shear stresses, this mechanism is referred to as *shearing*. Plastic deformation is essential, so this mechanism will generally be observed in face centered cubic crystals, which have many close-packed planes.

The fracture mechanism of direct shear specimen with guiding grooves in a rock was found experimentally to creating mode-II fracture (Rao et al., 2001). Macroscale ductile fracture is revealed by obvious changes in cross-section of the fracture part by shear lips on the fracture surface. Macroscale brittle fractures have fracture surfaces that are perpendicular to the applied load without evidence of prior deformation. Macroscale fracture surfaces can have a mixed-mode appearance (brittle-ductile or ductile-brittle). The brittle-ductile sequence is more common on the macroscale, while the appearance of the ductile portion is typically microscale in a ductile-brittle sequence. Zr-based metallic glasses always fail in a pure shear mode, whereas Co-based metallic glasses often break into small particles or powder, exhibiting a fragmentation mode (Zhang, Z.F. et al., 2006). The difference in the failure modes for the two glassy alloys indicates that different mechanisms control the fracture processes, which can be described by a combined effect of surface energy, cleavage strength, fragmentation coefficient, and fracture mode factor (ratio of shear stress to cleavage strength).

1.5.6.3 Cleavage Fracture

When plastic deformation at the crack tip is prohibited, the crack can travel through grains by splitting atomic bonds in lattice planes. This is called *intra- or trans-granular cleavage*. When the crack propagates along grain boundaries, it is referred to as *inter-granular cleavage*. This cleavage fracture will prevail in materials with little or no close-packed planes, having HCP (hexagonal close-packed (HCP) or body-centered cubic (BCC) crystal structure. It will also be observed when plastic deformation is prohibited

due to low temperature or high strain rate. Inter-granular cleavage will be found in materials with weak or damaged grain boundaries.

If the ratio of the atomic cohesive strength, σ_{R} , to the macroscopic yield strength, σ_{N} is greater than 4.0, crack-bridging models within the framework of continuum plasticity were found to predict that the crack blunts, limiting the near-tip stress to several times the yield strength (Needleman, 1987, 1990a; Varias et al., 1990; Tvergaard et al., 1992). Suo et al. (1993) proposed a theoretical approach for cleavage cracking surrounded by pre-existing dislocations, which emit from the crack front. The fracture process comprised atomic decohesion and background dislocation motion.

A typical micromechanism of brittle fracture is referred to as cleavage, where the atoms are gradually separated by tearing along the fracture plane very rapidly (Pokluda and Andrea, 2010). Brittle fracture in metallic materials occurs only when a pure cleavage or inter-granular decohesion takes place. Microscopically smooth cleavage cracks, observed in ferrite at very low temperatures, possess a surface energy of 14 J/m² which is much higher than that of about 1 J/m² related to the lower-bound benchmark for ideal cleavage cracks. A satisfactory explanation gives the cleavage mechanism based on alternative short-range dislocation slip proposed by Knott (2008).

The effect of the welding cycle on the fracture toughness properties of high strength low alloy (HSLA) steels was examined by means of thermal simulation of heataffected zone microstructures (Lambert-Perlade et al., 2004). Tensile tests on notched bars and fracture toughness tests at various temperatures are performed together with fracture surface observations and cross-sectional analyses. The influence of martensite-austenite (M-A) constituents and of crystallographic bainite packets on cleavage fracture micromechanisms was manifested as a function of temperature. Ravichandran et al. (1991) suggested that cleavage crack retardation at α/β interfaces in Widmanstatten titanium alloys could result from a conjoint action of thickness, ductility, and cyclic softening effects of β phase in addition to strain partitioning, hydride induced cracking effects. The thickness (volume fraction) and ductility of β phase and hydride induced cracking were found to be primarily responsible for cleavage crack arrest at thick β layers. It was revealed experimentally that the critical event for cleavage fracture is the unstable extension of a ferrite grainsized crack in specimens of C-Mn base and weld steel (Chen, J.H. and Wang, 1994). The main factor promoting the transition from the fibrous crack to cleavage was found to be the increase of the local tensile stress ahead of the crack, which was caused by the increase of the triaxiality of stress and the apparent normal stress in the remaining ligament. The considerable scattering of toughness values in the transition temperature region was found to be due to the random variation of the widths of the tips of the fibrous cracks during their extension and the random distribution of the weakest constituents in the microstructure.

1.5.6.4 Crazing Fracture

Crazing is manifested by a network of fine cracks on the surface of a material. Crazing frequently precedes fracture in some glassy thermoplastic polymers. It occurs in regions of high hydrostatic tension, or in regions of much localized yielding, which leads to the formation of interpenetrating microvoids and small fibrils. If an applied tensile load is sufficient, these bridges elongate and break, causing the microvoids to grow and then cracks begin to form.

A polymer fails either through deformation without change of volume, referred as shear, or deformation accompanied by volume increase referred as crazing (Kausch, 1987). Crazing was first described morphologically by Kambour (1973) and is initiated when the external stretch causes a microscopic void to open up at a stress concentration created by a pre-created notch, a heterogeneity in the molecular network, or a foreign particle. The probability of microscopic voids occurring is dependent on the local stress situation. Kausch et al. (2003) studied the effect of intrinsic variables on local molecular motions and on the competition between chain scission, disentanglement, and segmental slip, which in turn determine the dominant mode of instability and plastic behavior. Above a critical molecular weight, toughness depends strongly on the entanglement density; a positive effect of the intensity of sub- T_g relaxations (where T_g is the glass transition temperature) and in-chain cooperative motions on the toughness of these materials is clearly evident. Kramer (2005) proposed that in the craze nucleation mechanism, plane strain is more likely to open up such voids, than plane stress. Van Melick et al. (2003) found that the critical hydrostatic stress is in the order of the van der Waals surface energy of 40 mJ/m² and it increases with increasing network density.

Crazing was initially a phenomenon that was reported solely for glassy, amorphous polymers but it also occurs in semi-crystalline polymers as reported by Plummer et al. (1994, 2001) and Thomas et al. (2007). It is observed that the typical fibril sizes tend to be an order of magnitude coarser in the case of semi-crystalline polymers (200 nm) compared to amorphous polymers (20 nm). The experimentally observed presence of two brittle-ductile transitions, one at low temperature or high strain rates, linked with chain scission which dominates crazing, the other at elevated temperatures or low strain rates which involves disentanglement crazing provided an explanation of the polymer network response. The relation between these two brittle-ductile transitions and the major transition temperatures for molecular mobility such as the glass transition and the crystal α relaxation temperature were discussed by Deblieck et al. (2011), who demonstrated that the continuum model and the physicochemical specifications used to describe craze propagation in amorphous glassy polymers are not limited to amorphous polymers.

Boundary-Layer Effect of Composites 1.6

1.6.1 Introduction

The problem of the boundary-layer effects is due to interactions of geometric discontinuities of the composite and materials discontinuities through the laminate thickness. It was found to occur only within a very local region near the geometric boundaries of a composite laminate. It is frequently referred to as boundary-layer effect or free-edge effect. This problem is unique to composite laminates and not generally observed in homogeneous solids. Layered structural elements in lightweight constructions may suffer from severe stress concentrations of an interlaminar character which is not properly reflected by classical laminate plate theory (Ashton and Whitney, 1970; Bert, 1975; Tsai and Hahn, 1980; Herakovich, 1998a; Jones, 1998; Reddy, 2004). The classical laminate plate theory is a two-dimensional theory and assumes a layer-wise plane state of stress in conjunction with the kinematic assumptions of the classical plate theory of Kirchhoff. In the presence of irregularities, the resultant stress fields in general are of a pronounced three-dimensional nature and on a theoretical basis may even become singular. An example of this class of stress localization problems is the well-known boundary-layer or free-edge effect, which is an example of stress localization and has been the subject of several investigations for many years.

The behavior of a multi-layered fiber-reinforced composite laminate near its geometric boundaries has been the subject of extensive experimental and analytical studies (e.g. Pipes and Pagano, 1970, 1974; Puppo and Evensen, 1970; Pagano and Pipes, 1971; Pipes and Daniel, 1971; Isakson and Levy, 1971; Rybicki, 1971, Pipes et al., 1973; Whitney, 1973; Pagano, 1974; Tang, 1975; Tang and Levy, 1975; Hsu and Herakovich, 1977; Rybicki et al., 1977; Wang, J.T.S. and Dickson, 1978, Wang, S.S. and Choi, 1981, 1982a, 1982b; Wang, S.S. and Yuan, 1983). These studies revealed that complex stress states with rapid change of gradients occur along the edges of composite laminates. For example, Pipes and Pagano (1974) considered symmetric angle-ply laminates under uniaxial tension by approximating the displacement field with Fourier series. Convergence investigations showed that a large number of series terms was needed to achieve reasonably accurate results. This led Pipes and Pagano (1974) to believe the possible existence of a singularity for the interlaminar shear stress at the free edge of angle-ply laminates. Tang (1975) and Tang and Levy (1975) used layer-wise series expansions for the stress field with respect to one half of the thickness of the respective layers. An approximation of zero-order was obtained in closed-form expressions for the complete stress field in the considered laminates. These expressions satisfied the conditions of equilibrium and traction-free edges together with continuity of displacements. However, the interlaminar shear stresses did not satisfy the conditions of traction-free laminate surfaces and were not continuous through the laminate thickness. Conti and De Paulis (1985) extended the work of Pagano and Pipes (1971, 1973) for the stress approximation in angle-ply laminates and the calculation of interlaminar stress distributions through the laminate thickness.

Pagano (1978a, 1978b) developed an approximate analytical approach to predict the stress field within the composite laminates as well as near the free edges. Soni (1982), Pagano and Soni (1983), and Soni and Pagano (1983) developed a global-local model based on a higher-order theory approach by dividing the laminate into global and local regions. The methodology for the local region was based on the work of Pagano (1978a, 1978b). In this region the approach allows a refined analysis of the stress fields in the vicinity of free edges, whereas the global region is modeled with an equivalent single layer approach introduced by Whitney and Sun (1973). Wang, A.S.D. and Crossman (1977) solved the problem proposed by Pipes and Pagano (1970) by means of the finite element method. A special-purpose hybrid-stress finite element was presented by Spikler et al. (1981) and Spikler and Engelmann (1986). This hybrid algorithm ensures exact traction-free conditions at the free edges of symmetric laminates under uniform axial strain. In contrast with the previously established notion about the stress singularity at the free edges, by increasing the mesh refinement they showed that all stress components at the free edges converged to finite values.

It was shown that the boundary-layer effect is three-dimensional in nature and is considered as one of the most fundamental and important problems in the mechanics and mechanical behavior of composite laminates. The high interlaminar stresses are known to be the dominant factor causing delamination. Wang, S.S. and Choi (1981, 1982a, 1982b) concluded that the boundary-layer or free-edge stress field in a composite

laminate is inherently singular in nature due to the geometric and material discontinuities. Furthermore, the order of boundary-layer stress singularity can be determined by solving for the transcendental characteristic equation obtained from the homogeneous solution of the governing partial differential equations. The boundary-layer stress singularity depends only upon material's elastic constants and the fiber orientations of adjacent plies in composite laminates. Bar-Yoseph and Pian (1981) developed an analytical method in which the stress field could be found by minimization of the complementary potential energy in the boundary-layer region. Altus et al. (1980) developed a three-dimensional finite difference scheme to examine simultaneously all three interlaminar stresses. Kassapoglou and Lagace (1986, 1987) presented an analysis of free-edge stresses representing the stresses as products of in-plane exponential terms and polynomials through the thickness. Later, Kassapoglou (1989, 1990) considered free-edge stresses in bending, and estimated the failure of laminates due to interlaminar stresses by adequate failure criteria. Herakovich (1989b), Kant and Swaminathan (2000), and Mittelstedt and Becker (2004a, 2007b) presented valuable assessments of the problem of free-edge effects and stress concentration.

1.6.2 Analytical Treatment

Consider a composite laminate of finite width that is subjected to the applied force, P_z , bending moments M_x , and M_y , and twisting moment, M_t , all acting at the ends, as shown in Figure 1.14. The end effect is neglected by virtue of the Saint Venant principle. In this case, the stresses in the laminate are independent of the z-coordinate. Introducing the Airy stress functions (Lekhnitskii's stress potentials), $\Phi = \Phi(x,y)$ and $\Psi = \Psi(x,y)$, which satisfies the plane stress in the absence of body forces, such that (Lekhnitskii, 1963)

$$\sigma_x = \frac{\partial^2 \Phi}{\partial y^2}, \quad \sigma_y = \frac{\partial^2 \Phi}{\partial x^2}, \quad \sigma_{xy} = -\frac{\partial^2 \Phi}{\partial x \partial y}$$
 (1.69a)

$$\tau_{xz} = \frac{\partial \Psi}{\partial y}, \quad \tau_{yz} = -\frac{\partial \Psi}{\partial x}$$
(1.69b)

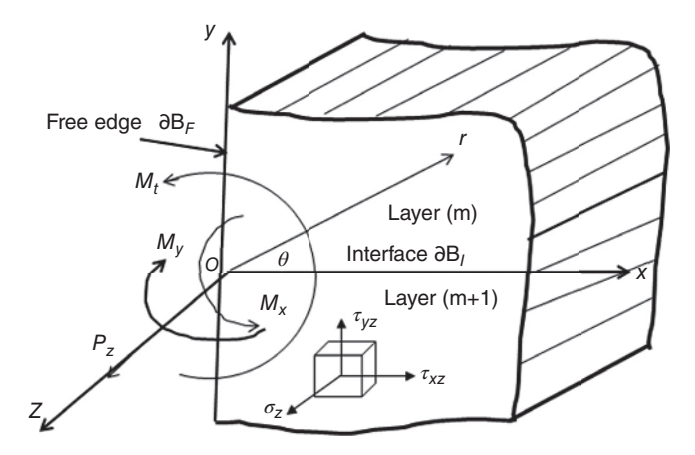


Figure 1.14 Schematic diagram of composite laminate of finite width subjected to the applied force, P_{z_i} bending moments, M_x and M_y and twisting moment, M_{t_i} all acting at the ends.

Wang, S.S. and Choi (1981) showed that the governing equations of equilibrium are given by the partial differential equations

$$L_3\Phi + L_2\Psi = -2A_4 + A_1S_{34} - A_2S_{35} \tag{1.70a}$$

$$L_4 \Phi + L_3 \Psi = 0 \tag{1.70b}$$

where L_2 , L_3 , and L_4 are linear differential operators given by the expressions

$$L_2 = S_{44} \frac{\partial^2}{\partial x^2} - 2S_{45} \frac{\partial^2}{\partial x \partial y} + S_{55} \frac{\partial^2}{\partial y^2}$$
 (1.71a)

$$L_{3} = -S_{24} \frac{\partial^{3}}{\partial x^{3}} + \left(S_{25} + S_{46}\right) \frac{\partial^{3}}{\partial x^{2} \partial y} - \left(S_{14} + S_{56}\right) \frac{\partial^{3}}{\partial x \partial y^{2}} + S_{15} \frac{\partial^{3}}{\partial y^{3}}$$
(1.71b)

$$L_{4} = S_{22} \frac{\partial^{4}}{\partial x^{4}} - 2S_{26} \frac{\partial^{4}}{\partial x^{3} \partial y} + \left(2S_{12} + S_{66}\right) \frac{\partial^{4}}{\partial x^{2} \partial y^{2}} - 2S_{16} \frac{\partial^{4}}{\partial x \partial y^{3}} + S_{11} \frac{\partial^{4}}{\partial y^{4}}$$
(1.71c)

where S_{ij} is the compliant tensor defined by the stress–strain relationship

$$\varepsilon_i = S_{ii}\sigma_i, i, j = 1, 2, 3, 4, 5, 6$$
 (1.72)

where repeated subscript indicates summation. With reference to Figure 1.14, let the edges of a composite laminate, ∂B_F , be traction free and the interface of the mth and (m+l)th plies be a straight line meeting the traction-free edge at a right angle. In this case, we can obtain the following boundary conditions along ∂B_F :

$$\sigma_x = \tau_{xy} = \tau_{xz} = 0 \tag{1.73}$$

The conditions at the ends of the composite laminate may have the form, from the statically equivalent loads,

$$\iint_{B} \tau_{xz} dx dy = 0, \quad \iint_{B} \tau_{yz} dx dy = 0, \quad \iint_{B} \sigma_{z} dx dy = P_{z},
\iint_{B} \sigma_{z} y dx dy = M_{x}, \quad \iint_{B} \sigma_{z} x dx dy = M_{y}, \quad \iint_{B} (\tau_{yz} x - \tau_{xz} y) dx dy = M_{t}$$
(1.74)

where *B* denotes the entire area of the cross-section.

Now consider a portion of the laminate cross-section composed of the mth and (m+l)th fiber-reinforced laminae, as shown in Figure 1.14. Assuming that the plies are perfectly bonded along the interface ∂B , we can immediately establish the continuity conditions of the stresses and displacements along the interface as

$$\sigma_x^{(m)} n_x^{(m)} + \tau_{xy}^{(m)} n_y^{(m)} = -\sigma_x^{(m+1)} n_x^{(m+1)} - \tau_{xy}^{(m+1)} n_y^{(m+1)}$$
(1.75a)

$$\tau_{xy}^{(m)} n_x^{(m)} + \sigma_y^{(m)} n_y^{(m)} = -\tau_{xy}^{(m+1)} n_x^{(m+1)} - \sigma_y^{(m+1)} n_y^{(m+1)}$$
(1.75b)

$$\tau_{xz}^{(m)} n_x^{(m)} + \tau_{yz}^{(m)} n_y^{(m)} = -\tau_{xz}^{(m+1)} n_x^{(m+1)} - \tau_{yz}^{(m+1)} n_y^{(m+1)}$$
(1.75c)

$$u^{(m)} = u^{(m+1)}, \quad v^{(m)} = v^{(m+1)}, \quad w^{(m)} = w^{(m+1)},$$
 (1.75d)

where the superscripts denote the mth and (m+l)th plies in a composite laminate. n_r and n_{ν} are components of unit outward normal to the interface.

The governing equations (1.70a) and (1.70b) are coupled linear partial differential equations with constant coefficients related to the anisotropic elastic constants of each individual lamina. The homogeneous solution of these equations subject to the nearfield boundary conditions and interface continuity conditions was obtained by Wang, S.S. and Choi (1981). The homogeneous boundary conditions and interface continuity conditions also provide the information for determining the free-edge stress singularity in a composite laminate. According to Lekhnitskii (1963), the homogeneous solution for the governing partial differential equations may be written in the general form

$$\Phi(x,y) = \sum_{k=1}^{6} \Phi_k(x + \mu_k y), \quad \Psi(x,y) = \sum_{k=1}^{6} \eta_k \Phi'_k(x + \mu_k y), \tag{1.76}$$

where a prime denotes differentiation with respect to its argument, and the coefficients μ are the roots of the following algebraic characteristic equation

$$\ell_4(\mu)\ell_2(\mu) - \ell_3^2(\mu) = 0 \tag{1.77a}$$

and

$$\eta_k = -\frac{\ell_3(\mu_k)}{\ell_2(\mu_k)} = -\frac{\ell_4(\mu_k)}{\ell_3(\mu_k)} \tag{1.77b}$$

where

$$\ell_{2}(\mu) = S_{55}\mu^{2} - 2S_{45}\mu + S_{44}$$

$$\ell_{3}(\mu) = S_{15}\mu^{3} - (S_{14} + S_{56})\mu^{2} + (S_{25} + S_{46})\mu + S_{44}$$

$$\ell_{4}(\mu) = S_{11}\mu^{4} - 2S_{16}\mu^{3} + (2S_{12} + S_{66})\mu^{2} - S_{26}\mu + S_{22}$$

It was indicated by Wang and Choi that equation (1.77a) cannot have a real root (thus, μ_k have to appear as complex conjugates), and Φ_k , are analytic functions of the complex variables $Z_k = x + \mu_k y = r(e^{i\theta} + \lambda_k e^{-i\theta})/(1 + \lambda_k)$ with $\lambda_k = (1 + i\mu_k)/(1 - i\mu_k)$. The r and θ are components of polar coordinates. Substituting equations (1.76) into equations (1.69a) and (1.69b), the homogeneous solutions for stresses may be expressed in terms of $\Phi_k(Z_k)$, i.e.

$$\sigma_x^{(h)} = \sum_{k=1}^6 \mu_k^2 \Phi_k^{"}(Z_k), \qquad \sigma_y^{(h)} = \sum_{k=1}^6 \Phi_k^{"}(Z_k), \tag{1.78a,b}$$

$$\tau_{yz}^{(h)} = -\sum_{k=1}^{6} \eta_k^2 \Phi_k^{"}(Z_k), \quad \tau_{xz}^{(h)} = \sum_{k=1}^{6} \mu_k \eta_k \Phi_k^{"}(Z_k), \quad \tau_{xy}^{(h)} = -\sum_{k=1}^{6} \mu_k \Phi_k^{"}(Z_k), \quad (1.78\text{c,d,e})$$

We can express the stress functions $\Phi_k(Z_k)$ in the form

$$\Phi_k(Z_k) = C_k Z_k^{\varpi+2} / \left[(\varpi+1)(\varpi+2) \right], \tag{1.79}$$

where C_k and ϖ are arbitrary complex constants to be determined. Substituting equation (1.79) into equations (1.78) gives

$$\sigma_{x}^{(h)} = \sum_{k=1}^{3} \left(C_{k} \mu_{k}^{2} Z_{k}^{\varpi} + C_{k+3} \overline{\mu}_{k}^{2} \overline{Z}_{k}^{\varpi} \right), \qquad \sigma_{y}^{(h)} = \sum_{k=1}^{3} \left(C_{k} Z_{k}^{\varpi} + C_{k+3} \overline{Z}_{k}^{\varpi} \right),
\tau_{yz}^{(h)} = -\sum_{k=1}^{3} \left(C_{k} \eta_{k} Z_{k}^{\varpi} + C_{k+3} \overline{\eta}_{k} \overline{Z}_{k}^{\varpi} \right), \qquad \tau_{xz}^{(h)} = \sum_{k=1}^{3} \left(C_{k} \eta_{k} \mu_{k} Z_{k}^{\varpi} + C_{k+3} \overline{\eta}_{k} \overline{\mu}_{k} \overline{Z}_{k}^{\varpi} \right), \qquad (1.80)$$

where the superscript (h) denotes homogeneous solution and the overbar denotes the complex conjugate of the associate variable. Wang, S.S. and Choi (1981) obtained the corresponding expressions for displacements. The homogeneous solutions are required to satisfy the homogeneous boundary conditions and interface continuity conditions. This leads to a standard eigenvalue problem for determining the values of ϖ . It is noted that ϖ generally appears as a set of complex conjugates, which enable us to make equations (1.66) real functions by superposition. Furthermore, the value of ϖ is required to satisfy the condition $Re[\varpi] > -1$ to ensure bounded values of displacement components at the origin, where Re represents the real part of ϖ . Equations (1.80) can be transformed into polar coordinates (r, θ) to take the form

$$\sigma_{\theta\theta} = \sum_{k=1}^{3} \left(C_{k} H_{1k} Z_{k}^{\varpi} + C_{k+3} \bar{H}_{1k} \bar{Z}_{k}^{\varpi} \right), \qquad \tau_{\theta z} = \sum_{k=1}^{3} \left(C_{k} H_{2k} Z_{k}^{\varpi} + C_{k+3} \bar{H}_{2k} \bar{Z}_{k}^{\varpi} \right),
\tau_{\theta r} = \sum_{k=1}^{3} \left(C_{k} H_{3k} Z_{k}^{\varpi} + C_{k+3} \bar{H}_{3k} \bar{Z}_{k}^{\varpi} \right), \qquad \sigma_{rr} = \sum_{k=1}^{3} \left(C_{k} H_{4k} Z_{k}^{\varpi} + C_{k+4} \bar{H}_{2k} \bar{Z}_{k}^{\varpi} \right), \qquad (1.81)$$

$$\tau_{rz} = \sum_{k=1}^{3} \left(C_{k} H_{5k} Z_{k}^{\varpi} + C_{k+3} \bar{H}_{5k} \bar{Z}_{k}^{\varpi} \right), \qquad (2.81)$$

where Z_k are defined in the polar coordinates and $H_{1k} = (\mu_k \sin \theta + \cos \theta)^2$, $H_{2k} = -\eta_k$ $(\mu_k \sin \theta + \cos \theta), H_{3k} = -(\mu_k \sin \theta + \cos \theta)(\mu_k \cos \theta - \sin \theta), \text{ and } H_{4k} = (\mu_k \cos \theta - \sin \theta)^2.$ The boundary conditions (73) along the free-edges of the mth and (m+l)th plies in terms of polar coordinates take the form

$$\sigma_{\theta\theta}^{(m)} = \tau_{\theta z}^{(m)} = \tau_{r\theta}^{(m)} = 0 \quad \text{on} \quad \theta = \pi/2$$

$$\sigma_{\theta\theta}^{(m+1)} = \tau_{\theta z}^{(m+1)} = \tau_{r\theta}^{(m+1)} = 0 \quad \text{on} \quad \theta = -\pi/2$$

$$(1.82)$$

The continuity conditions (75) along the ply interface take the form

$$\begin{cases}
\sigma_{\theta\theta}^{(m)}, \tau_{\theta z}^{(m)}, \tau_{r\theta}^{(m)}, u_r^{(m)}, u_{\theta}^{(m)}, u_z^{(m)} \\
= & \left\{ \sigma_{\theta\theta}^{(m+1)}, \tau_{\theta z}^{(m+1)}, \tau_{r\theta}^{(m+1)}, u_r^{(m+1)}, u_{\theta}^{(m+1)}, u_z^{(m+1)} \right\} \quad \text{on} \quad \theta = 0
\end{cases}$$
(1.83)

The homogeneous boundary conditions (82) and the continuity conditions (83) can be explicitly written in the form

$$\sum_{k=1}^{3} \left\{ C_k^{(m)} H_{jk}^{(m)} \left(\frac{\pi}{2} \right) \left[\Omega_k^{(m)} \left(\frac{\pi}{2} \right) \right]^{m} + C_{k+3}^{(m)} \overline{H_{jk}^{(m)} \left(\frac{\pi}{2} \right)} \left[\overline{\Omega_k^{(m)} \left(\frac{\pi}{2} \right)} \right]^{m} \right\} = 0$$
 (1.84a)

$$\sum_{k=1}^{3} \left\{ C_k^{(m+1)} H_{jk}^{(m+1)} \left(-\frac{\pi}{2} \right) \left[\Omega_k^{(m+1)} \left(-\frac{\pi}{2} \right) \right]^{\sigma} + C_{k+3}^{(m+1)} \overline{H_{jk}^{(m+1)} \left(-\frac{\pi}{2} \right)} \left[\overline{\Omega_k^{(m+1)} \left(-\frac{\pi}{2} \right)} \right]^{\sigma} \right\} = 0$$
(1.84b)

$$\sum_{k=1}^{3} \left\{ \left[C_{k}^{(m)} \Gamma_{rk}^{(m)} + C_{k+3}^{(m)} \overline{\Gamma}_{rk}^{(m)} \right] - \left[C_{k}^{(m+1)} \Gamma_{rk}^{(m+1)} + C_{k+3}^{(m+1)} \overline{\Gamma}_{rk}^{(m+1)} \right] \right\} = 0$$
 (1.84c)

where $j=1,2,3; \quad r=1,2,3,4,5,6.$ $H_{jk}^{(m)}(\pi/2)$ and $H_{jk}^{(m)}(\pi/2)$ are the values of H_{jk} evaluated at $\theta=(\pi/2)$ and $\theta=(-\pi/2)$, respectively. The functions $\Omega_k^{(m)}(\theta)$ are defined by the expression $\Omega_k(\theta)=(e^{i\theta}+\lambda_k e^{-i\theta})/(1+\lambda_k)$, $\Gamma_{1k}=1$, $\Gamma_{2k}=\eta_k$, $\Gamma_{3k}=\mu_k$, $\Gamma_{4k}=p_k$, $\Gamma_{5k}=q_k$, $\Gamma_{6k}=t_k$, and $p_k=S_{11}\mu_k^2+S_{12}-S_{14}\eta_k+S_{15}\eta_k\mu_k-S_{16}\mu_k$, $q_k=S_{12}\mu_k+S_{22}/\mu_k-S_{24}\eta_k/S_{24}\eta_k$ $\mu_k + S_{25}\eta_k - S_{26}$, and $t_k = S_{14}\mu_k + S_{24} / \mu_k - S_{44}\eta_k / \mu_k + S_{45}\eta_k - S_{46}$. From equation (1.84c) we can write the coefficients $C_k^{(m)}$ in terms of $C_k^{(m+1)}$ in the form

$$C_k^{(m)} = a_{ks}C_k^{(m+1)}, \quad k, s = 1, 2, ..., 6$$
 (1.85)

In this case equation (1.84a) takes the form

$$\sum_{s=1}^{6} \left\{ C_s^{(m+1)} \sum_{k=1}^{3} \left\{ H_{jk}^{(m)} \left(\frac{\pi}{2} \right) \mathbf{a}_{ks} \left[\Omega_k^{(m)} \left(\frac{\pi}{2} \right) \right]^{\omega} + \overline{H_{jk}^{(m)} \left(-\frac{\pi}{2} \right)} \mathbf{a}_{(k+3)s} \left[\overline{\Omega_k^{(m)} \left(-\frac{\pi}{2} \right)} \right]^{\omega} \right\} \right\} = 0 \quad (1.86)$$

Equations (1.84b) and (1.86) constitute a system of homogeneous linear algebraic equations in $C_k^{(m+1)}$. The existence of a non-trivial solution for $C_k^{(m+1)}$ requires the vanishing of the coefficient determinant

$$\Delta |\varpi| = 0 \tag{1.87}$$

where $\Delta |\varpi|$ is a 6×6 matrix involving ϖ in a transcendental form. Thus, equation (1.83) is a transcendental characteristic equation for the standard eigenvalue problem. It has a very complicated structure, as can be seen from the coefficients of $C_k^{(m+1)}$ in equations (1.84) and (1.86), and the detailed expression for $\Delta |\varpi|$ may be obtained using Mathematica. The investigation of the characteristic equation requires the employment of standard numerical techniques. The eigenvalues ϖ_n obtained from the numerical solution of equation (1.87) give important information concerning the behavior of the edge stresses and displacements. Due to the positive definiteness of strain energy of the elastic structure and the condition $Re[\varpi] > -1$, the eigenvalue of ϖ_n is bounded by the condition

$$-1 < \operatorname{Re}\left[\varpi_n\right] > -1 < 0 \tag{1.88}$$

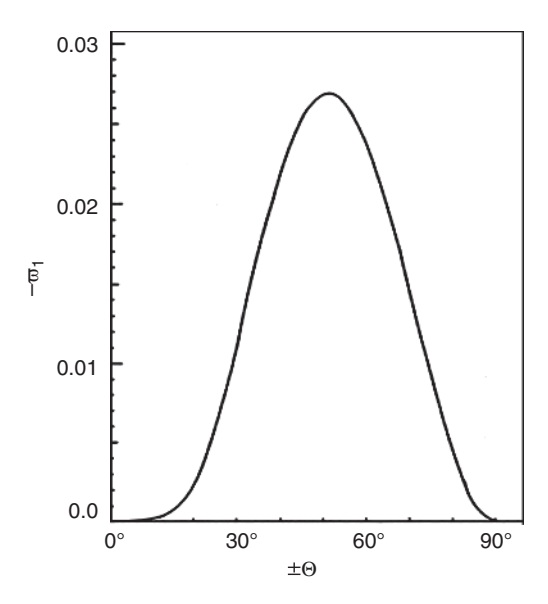


Figure 1.15 Dependence of the eigen-value ϖ_1 on the fiber orientation angle Θ of ply graphite-epoxy composite. (Wang and Choi, 1981)

This condition characterizes the order of the inherent singularity of the boundary-layer or free-edge stresses in a composite laminate.

For the commonly used $\pm\Theta$ angle-ply graphite-epoxy composite the order of the boundary-layer stress singularity is a function of the fiber orientation Θ . Wang, S.S. and Choi (1981, 1982c) numerically estimated the values of ϖ_1 for each of the $\pm\Theta$ fiber orientations and their results are plotted in Figure 1.15, which reveals that the composite free edge associated with the laminate of an approximately ($\pm 51^\circ$) ply orientation possesses the strongest boundary-layer stress singularity. As the Θ changes to either directions, the order of the stress singularity ϖ_1 decreases rapidly. Its value converges to zero for the cases of $\Theta=0^\circ$ or $\Theta=90^\circ$, since the two plies become identical with orthotropic elastic properties.

Pipes et al. (1973), Herakovich et al. (1979), and Sun and Zhou (1990) found that the high stresses developed in the boundary-layer region coupled with the low interlaminar strength are responsible for the initiation and growth of local heterogeneous damage in the forms of interlaminar (delamination) and intralaminar (transverse cracking) fracture in composite laminates under static loading. Christensen (1979) and Wilkins, et al. (1982) found that these stresses have significant effects on the long-term strength of composite laminates under cyclic fatigue loading. Yin (1994a, 1994b) used a variational approach involving Lekhnitskii's stress functions for the assessment of free-edge stresses in laminates under uniaxial extension, bending, and torsion. The fundamental nature of the boundary layer effects in multi-layer composite laminates was studied by Michel et al. (1996). The structure of the boundary layer field, based on the theory of anisotropic elasticity and on Lekhnitskii's (1963) complex variable stress potentials were presented. The order of singularity included in the formulation of the stress and displacement fields at composite laminate edges

was studied through some examples of structures and materials including delamination and free edges. The results revealed the strong influence of several parameters on singularity orders and therefore on stresses.

The finite-difference approach was used in the investigation of the edge effect in a composite laminate subjected to a piecewise constant load by Guz et al. (1986). The evaluation of the zone of the edge effect was obtained in terms of the ratio of the elastic properties of the isotropic layers and their geometric characteristics. An eigen-function expansion was developed for the determination of the three-dimensional stress field in the neighborhood of the intersection of the free edge of a hole and an interface in a laminated composite plate by Folias (1992). For transversely isotropic laminae, the stress field was shown to possess a weak singularity whose strength depends on the material constants, the fiber orientations of the two adjacent laminae, and the polar angle. Results for $[0^{\circ}/90^{\circ}]$, $[0^{\circ}/70^{\circ}]$, $[0^{\circ}/45^{\circ}]$, and $[0^{\circ}/20^{\circ}]$ were presented, and the best and worst fiber orientations were identified. The circumferential stress was shown to possess a small jump across the interface. The edge-zone equation of Mindlin-Reissner plate theory for composite plates laminated of transversely isotropic layers was studied by Nosier et al. (2001). Analytical solutions were obtained for both circular sector and completely circular plates with various boundary conditions. The interlaminar stresses close to the free edges of general cross-ply composite laminates based on higher-order equivalent single-layer theory was determined by Sarvestani and Naghashpour (2014). The laminates with finite dimensions were subjected to a bending moment, an axial force, and/or a torque for investigation. Full three-dimensional stresses in the interior and the boundary-layer regions were determined. The computed results were compared with those obtained from Reddy's layer-wise theory. It was found that higher-order equivalent single-layer theory precisely predicts the interlaminar stresses near the free edges of laminates.

The three-dimensional stress field, developed at the free-edge of an externally loaded composite laminated plate, was found to exist in a thin layer close to the free-edge layer. It may cause delamination, well before the expected failure of the matrix or fibers. It is mainly explained by the mismatch of the elastic material properties between two adjacent dissimilar laminate layers. The free-edge effect was characterized by the concentrated three-dimensional and singular stress fields at the free edges in the interfaces between two layers of composite laminates. An assessment of modeling techniques and the effect of stress field for symmetric laminates subjected to different load condition was presented by Soni and Pagano (1987), Murthy and Chamis (1989), Bar-Yoseph and Ben-David (1991, 1995), and Mittelstedt and Becker (2004f, 2004g, 2007b). It was found that the edge effect is more dominant in tension than in bending loading for symmetric and unsymmetric laminates, and more pronounced for symmetric angle-ply than for unsymmetric angle-ply laminates. The main difficulty of analyzing unsymmetrically laminated shells is due to the coupling of different modes of loading and deflection.

The response of the shell to constant internal pressure was studied by Preissner and Vinson (2004), with particular attention given to the bending boundary layer near the ends using the ABAQUS finite element program. It was found that the extent of the bending boundary layer in the non-circular case is 2.5-4 times longer than that predicted by the classical equation, but the *intensity* of the bending boundary layer was reduced. An unusual compounding effect in boundary layer response for short noncircular shells was described.

Gu and Reddy (1992) developed a finite-element model based on the guasi-threedimensional elasticity theory of Pipes and Pagano (1970, 1974) to examine the effect of geometric nonlinearity on free-edge stress fields in composite laminates subjected to in-plane loads. It was found that the qualitative nature of the stresses remains the same as those obtained in the linear analysis, but the nonlinear stresses are larger in magnitude by 5-40%, depending on the laminate. However, in most cases the difference was found to be about 10%. Davi (1996) examined the stress fields in general laminates under uniform axial strain using the integral equation theory and boundary element method. An analytical, parametric study of the attenuation of bending boundary layers in balanced and unbalanced, symmetrically and unsymmetrically laminated thin cylindrical shells was presented by Nemeth and Smeltzer (2000) for nine contemporary material systems. It was found that the effect of anisotropy in the form of coupling between pure bending and twisting has a negligible effect on the size of the bending boundary-layer attenuation length of symmetrically laminated cylinders. Moreover, the results showed that the coupling of the membrane and flexural anisotropy and the anisotropy caused by unsymmetric lamination is generally unimportant with regards to the primary effect of the individual shell anisotropies on the bending boundarylayer decay length.

Numerical studies of corner singularities and possible fracture phenomena in corner regions were presented by Labossière and Dunn (2001) and Dimitrov et al. (2001, 2002a, 2002b, 2002c). For example, stress singularities in a laminated composite wedge under real three-dimensional corner effects were studied by Dimitrov et al. (2001, 2002a), who developed a numerical approach for the asymptotic analysis of the linearelastic solution in the neighborhood of some three-dimensional singular points. Their results revealed a strong dependence of the singular exponents on the wedge angle: for wedge angles smaller than π (convex wedges) the singularity is relatively weak, whereas for angles greater than π (concave wedges) the dominant singularity is significantly stronger and reaches quickly its minimum near 0.5. This means, that holes with sharp edges or concave corners are much more dangerous for composite structures than convex corners or edges. Carrera and Demasi (2002a, 2002b) presented an assessment of the accuracy of the finite-element mixed layer-wise formulations using the Reissner mixed variational theorem by comparing various results (including the interlaminar stresses) of several finite-element models and elasticity theory within composite laminates and sandwich plates.

Note that asymptotic solutions for a class of elasticity problems including stress singularities using an eigen-function expansion method were developed by Chaudhuri and Xie (1998, 2000), Xie and Chaudhuri (1998, 2001), and Chiu and Chaudhuri (2002) based on the work of Williams (1952). Performing a separation of variables for the displacements and formulating a power-law series for the radial components of the displacements, the order of the assumed power-law singularities was finally calculated from a set of eigen-equations that resulted from boundary and continuity conditions. Müller et al. (2002a, 2002b, 2003) expressed the in-plane stress and displacement field in the vicinity of unsymmetrically laminated bi-material notches by two complex analytical potentials.

The boundary layer effect in rectangular laminated plates was studied by Kumari and Kapuria (2011) and Kapuria and Kumari (2012), who used an efficient third-order zigzag theory. A Levy-type solution was obtained for rectangular plates, with two opposite edges hard-simply supported. While strong edge effects were observed at the free edges and soft-simply supported edges, no edge effect appears at the hard-simply supported edge. The effect of length to thickness ratio and aspect ratio on the boundary layer is investigated. The results are compared with those of the smeared third-order theory to ascertain the effect of inclusion of layer-wise terms in the displacement approximation of the zigzag theory. The effect of electromechanical coupling and electric boundary conditions on the distributions of stress resultants near the edges was studied. The effect of inclusion of layer-wise terms in the displacement approximation of the efficient layer-wise theory was examined by comparing the results with those of the coupled smeared third-order theory.

1.6.3 Thermal Loading Stress Field

The free-edge effect is characterized by three-dimensional and singular stress fields at the interfaces between dissimilar layers at the free edges of laminates under thermal, mechanical, or hygroscopic loadings. Free-edge stress fields exhibit steep stress gradients and rapidly decay with increasing distance from the laminate edges, until finally they vanish in the inner laminate regions. The amount of moisture held by hygroscopic materials is usually proportional to the relative humidity. Wang, S.S. and Choi (1982c) obtained complete solutions for the hygroscopic stresses in graphite-epoxy laminates with various fiber orientations and ply thicknesses. Both variables were shown to have significant effects on the development of in-plane and interlaminar hygroscopic stresses. Important parameters characterizing the boundary-layer behavior such as hygroscopic edge stress singularities and stress intensity factors were considered.

Thermal loadings were introduced by Webber and Morton (1993) and Morton and Webber (1993) who presented failure analyses of composites under mechanical and thermal load by applying the force-balance method in combination with adequate failure criteria. Additional terms for the consideration of the discontinuous change of the elastic material properties in the interfaces were introduced by Rose and Herakovich (1993). The additional terms took into account the local mismatches in Poisson's ratio and coefficient of mutual influence between adjacent layers. The influence of thermally induced residual stresses on the strength of composite materials together with the influence of adhesive layers between two adjacent laminate plies on free-edge stress fields with respect to the free-edge effect was studied by Wu (1990). Later, Wu (1992) examined $[\pm \theta]$ -symmetric laminates under combined thermal and mechanical loading. His analysis included the physical nonlinear behavior and the influence of fibreless transition layers. For the case of $[\pm \theta]$ -symmetric layups, the thermal stresses were found to have strengthening effect on the ultimate load of the laminate.

The influence of combined thermal and mechanical loads on free-edge stress fields was studied by Yin (1994c, 1997) and Kim and Atluri (1995). Yin considered the variation of thermal loads through the thickness as well as along the coordinate parallel to the interface. Thermal loads were assumed to vary linearly only through the thickness. Free exponential parameters in the assumed stress shapes were estimated by minimization of the total laminate complementary potential. The applicability of the described method was found to be limited to thin laminates with few layers. This limitation is due to the fact that by increasing number of plies the minimization of the energy functional requires the simultaneous solution of an increasing number of distinctly nonlinear equations for the unknown free parameters. On the other hand, Kim and Atluri (1995) employed an approach based on admissible function representations of stresses, which account for the effects of both global and local mismatches in Poisson's ratio and coefficient of mutual influence by applying respective mismatch terms in the stress representations. The unknown stress functions were determined by application of the principle of minimum complementary energy of the laminate. Zhang and Yeh (1998) used stress functions and a variational approach to the free-edge effect in symmetric laminates under combined mechanical and thermal load. Significant experimental evidence of singular stress fields in the vicinity of free laminate corners was reported by Herrmann and Linnenbrock (2002).

Free-edge effects in symmetric and unsymmetric cross-ply laminates under thermomechanical loading conditions were considered by Tahani and Nosier (2003) who used a layer-wise C^0 -continuous displacement formulation based on the work of Nosier et al. (1993). They used the layer-wise theory to study the interlaminar stresses near the free edges of the laminates. Based on the reduced elasticity displacement field of a long laminated composite plate, Nosier and Bahrami (2006, 2007) studied interlaminar stresses in anti-symmetric angle-ply laminates under extension and torsion. The interlaminar stresses near the free edges of generally laminated composite plates under extension were calculated by Nosier and Maleki (2008). The constant parameter appearing in the reduced displacement field, which describes the global rotational deformation of a laminate, was obtained by employing an improved first-order shear deformation theory. The effects of end conditions of laminates, fibers orientation angles and the stacking sequences of the layers within laminates, and geometric parameters on the boundarylayer stresses were considered. Free-edge effects in laminated, circular, cylindrical shell panels subjected to hygrothermal loading were studied by Nosier and Miri (2010) who used a displacement-based technical approach. Appropriate reduced displacement fields were determined for laminated composite shell panels with cross-ply and antisymmetric angle-ply layups. An equivalent single-layer shell theory was employed to determine the constant parameters appearing in the reduced displacement fields. The distributions of transverse shear and normal stresses in various shell panels under a uniform temperature change were numerically estimated.

Becker et al. (1999) and Mittelstedt and Becker (2003a) adopted a force-balance approach for the stress assessment at rectangular free corners of cross-ply laminates under thermal load. Mittelstedt and Becker (2004a, 2004b) presented a closed-form analytical method for approximate calculations of the stress fields in the vicinity of free rectangular corners of thermally loaded laminates with arbitrary layup. Their approach is essentially based on the force-balance method of Kassapoglou and Lagace (1986, 1987) and of Becker et al. (1999). Closed-form analytical methods for rectangular corners were developed by Becker et al. (1999, 2000, 2001), Mittelstedt and Becker (2003b, 2004a) employing the force-balance method formulation for cross-ply laminates and laminates with arbitrary layups, respectively. Mittelstedt and Becker (2003a) used displacement based equivalent single-layer theory approach for rectangular cross-ply laminates, and Mittelstedt and Becker (2004c, 2004e) displacement based layer-wise

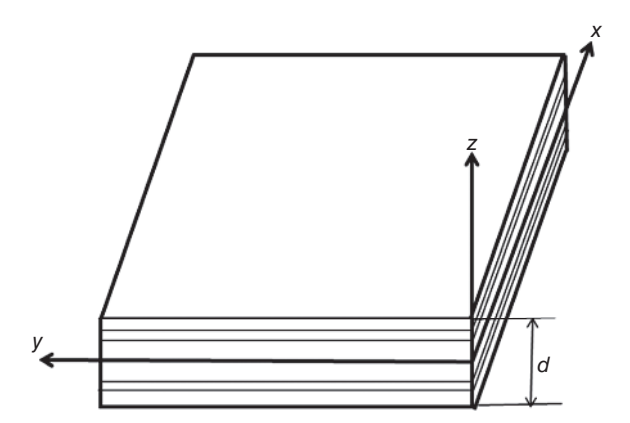


Figure 1.16 Schematic diagram of a laminate of arbitrary layup with n plies and the total thickness d showing the coordinate frame at the free-corner edge.

approach for rectangular cross-ply laminates based on the work of Reddy (1987). Numerical approaches employing the finite element method were carried out by Griffin (1988), Icardi and Bertetto (1995), and Herrmann and Linnenbrock (2002). The asymptotic analysis of the free-corner situation in layered structures was considered by Koguchi (1997) who used the boundary element approach. Finite element analysis was employed by Labossière and Dunn (2001), Nied and Ayhan (2001), Dimitrov (2002), Dimitrov et al. (2001, 2002a, 2002b, 2002c), and Dimitrov and Schnack (2002). Mittelstedt et al. (2004), and Mittelstedt and Becker (2004f, 2004g) used the scaled boundary finite element method.

Mittelstedt and Becker (2004b) considered a laminate of arbitrary layup with *n* plies and the total thickness d and is exposed to a constant temperature change ΔT , as shown in Figure 1.16. The three-dimensional stress field was studied in the interface between two arbitrarily chosen plies k and k+1 in a corner region. The functional dependence of all stress components was assumed in the product form

$$\sigma_{xx}^{k} = \left[1 - (1 + \varphi x)e^{-\phi x}\right] \left(1 + \lambda_{1}e^{-\lambda_{2}y}\right) \left(A_{1}^{(k)}z + A_{2}^{(k)}\right)
\sigma_{yy}^{k} = \left(1 + \varphi_{1}e^{-\varphi_{2}x}\right) \left[1 - (1 + \eta y)e^{-\eta y}\right] \left(A_{3}^{(k)}z + A_{4}^{(k)}\right)
\sigma_{xy}^{k} = \left(1 - e^{-\psi_{1}x}\right) \left[1 - e^{-\psi_{2}y}\right] \left(A_{5}^{(k)}z + A_{6}^{(k)}\right)$$
(1.89)

where φ , φ_1 , φ_2 , λ_1 , λ_2 , η , ψ_1 , and ψ_2 are constants to be determined using the variational principal. These constants describe the decaying rate of stress away from the free corner and edges of the laminate. The assumed in-plane stress distributions must satisfy the homogeneous boundary conditions for the intralaminar stresses, i.e.

$$\sigma_{xx}^{(k)}|_{x=0} = \sigma_{yy}^{(k)}|_{y=0} = \sigma_{xy}^{(k)}|_{x=0} = \sigma_{xy}^{(k)}|_{y=0} = 0$$
(1.90)

For the limiting case, $x, y \to \infty$, conditions for the stress field must also be satisfied. The exponential terms in equations (1.89) must vanish for $x, y \to \infty$. The constants A_i were obtained by the following adjustments:

$$\begin{split} A_{1}^{(k)} &= \frac{1}{d^{(k)}} \Big(\overline{\sigma}_{xxu}^{(k)} - \overline{\sigma}_{xxl}^{(k)} \Big), \quad A_{2}^{(k)} &= \overline{\sigma}_{xxl}^{(k)} - \frac{z_{(k-1)}}{d^{(k)}} \Big(\overline{\sigma}_{xxu}^{(k)} - \overline{\sigma}_{xxl}^{(k)} \Big) \\ A_{3}^{(k)} &= \frac{1}{d^{(k)}} \Big(\overline{\sigma}_{yyu}^{(k)} - \overline{\sigma}_{yyl}^{(k)} \Big), \quad A_{4}^{(k)} &= \overline{\sigma}_{yyl}^{(k)} - \frac{z_{(k-1)}}{d^{(k)}} \Big(\overline{\sigma}_{yyu}^{(k)} - \overline{\sigma}_{yyl}^{(k)} \Big) \\ A_{5}^{(k)} &= \frac{1}{d^{(k)}} \Big(\overline{\sigma}_{xyu}^{(k)} - \overline{\sigma}_{xyl}^{(k)} \Big), \quad A_{6}^{(k)} &= \overline{\sigma}_{xyl}^{(k)} - \frac{z_{(k-1)}}{d^{(k)}} \Big(\overline{\sigma}_{xyu}^{(k)} - \overline{\sigma}_{xyl}^{(k)} \Big) \end{split} \tag{1.91}$$

where the overbar denotes the classical laminate plate theory stresses, the subscripts u and l denote the values at the upper and lower interfaces of the k-th ply, respectively, $z_{(k-1)}$ is the thickness coordinate of the lower interface of the (k-1)-th layer, and $d^{(k)}$ is the thickness of the k-th ply. The three-dimensional equilibrium equations are

$$\frac{\partial \sigma_{xx}^{(k)}}{\partial x} + \frac{\partial \sigma_{xy}^{(k)}}{\partial y} + \frac{\partial \sigma_{xz}^{(k)}}{\partial z} = 0, \quad \frac{\partial \sigma_{xz}^{(k)}}{\partial x} + \frac{\partial \sigma_{yz}^{(k)}}{\partial y} + \frac{\partial \sigma_{zz}^{(k)}}{\partial z} = 0, \quad \frac{\partial \sigma_{xy}^{(k)}}{\partial x} + \frac{\partial \sigma_{yz}^{(k)}}{\partial y} + \frac{\partial \sigma_{yz}^{(k)}}{\partial z} = 0 \quad (1.92)$$

Equations (1.92) are used to determine the unknown interlaminar stress components by layer-wise integration:

$$\sigma_{xz}^{(k)} = -\int_{-d/2}^{z} \frac{\partial \sigma_{xx}^{(k)}}{\partial x} dz - \int_{-d/2}^{z} \frac{\partial \sigma_{xy}^{(k)}}{\partial y} dz$$

$$\sigma_{yz}^{(k)} = -\int_{-d/2}^{z} \frac{\partial \sigma_{xy}^{(k)}}{\partial x} dz - \int_{-d/2}^{z} \frac{\partial \sigma_{yy}^{(k)}}{\partial y} dz$$

$$\sigma_{zz}^{(k)} = -\int_{-d/2}^{z} \frac{\partial \sigma_{xz}^{(k)}}{\partial x} dz - \int_{-d/2}^{x_2} \frac{\partial \sigma_{yy}^{(k)}}{\partial y} dz$$

$$(1.93)$$

The continuity of the interlaminar stress components requires the following conditions to be satisfied:

$$\sigma_{xz}^{(k)}(x, y, z = z_{(k)}) = \sigma_{xz}^{(k+1)}(x, y, z = z_{(k)})$$

$$\sigma_{yz}^{(k)}(x, y, z = z_{(k)}) = \sigma_{yz}^{(k+1)}(xx, y, z = z_{(k)})$$

$$\sigma_{zz}^{(k)}(x, y, z = z_{(k)}) = \sigma_{zz}^{(k+1)}(x, y, z = z_{(k)})$$
(1.94)

The traction-free surfaces of the laminate must satisfy the following conditions:

$$\sigma_{xz}^{(1)}(x, y, z = -d/2) = \sigma_{xz}^{(n)}(x, y, z = d/2)$$

$$\sigma_{yz}^{(1)}(x, y, z = -d/2) = \sigma_{yz}^{(n)}(x, y, z = d/2)$$

$$\sigma_{zz}^{(1)}(x, y, z = -d/2) = \sigma_{zz}^{(n)}(x, y, z = d/2)$$
(1.95)

The interlaminar shear and normal stresses may be expressed in terms of linear combinations of stress functions obtained from integration of the in-plane stresses:

$$\begin{split} \sigma_{xz}^{(k)} &= -\Big(\varphi^2 x e^{-\varphi x}\Big) \Big(1 + \lambda_1 e^{-\lambda_2 y}\Big) \left(\frac{1}{2} A_1^{(k)} z^2 + A_2^{(k)} z + B_1^{(k)}\Big) \\ &- \Big(1 - e^{-\psi_1 x}\Big) \Big(\psi_2 e^{-\psi_2 y}\Big) \left(\frac{1}{2} A_5^{(k)} z^2 + A_6^{(k)} z + B_5^{(k)}\Big) \\ \sigma_{yz}^{(k)} &= -\Big(1 + \phi_1 e^{-\phi_2 x}\Big) \Big(\eta^2 y e^{-\eta y}\Big) \left(\frac{1}{2} A_3^{(k)} z^2 + A_4^{(k)} z + B_3^{(k)}\Big) \\ &- \Big(\psi_1 e^{-\psi_1 x}\Big) \Big(1 - e^{-\psi_2 y}\Big) \left(\frac{1}{2} A_5^{(k)} z^2 + A_6^{(k)} z + B_5^{(k)}\Big) \\ \sigma_{zz}^{(k)} &= \Big(\varphi^2 e^{-\varphi x} - \varphi^3 x e^{-\varphi x}\Big) \Big(1 + \lambda_1 e^{-\lambda_2 y}\Big) \left(\frac{1}{6} A_1^{(k)} z^3 + \frac{1}{2} A_2^{(k)} z^2 + B_1^{(k)} z + B_2^{(k)}\Big) \\ &+ \Big(\psi_1 e^{-\psi_1 x}\Big) \Big(\psi_2 e^{-\psi_2 y}\Big) \left(\frac{1}{3} A_5^{(k)} z^3 + A_6^{(k)} z^2 + 2 B_5^{(k)} z + B_6^{(k)}\Big) \end{split}$$

where the constants B_i are given by the following expressions

$$\begin{split} B_{1}^{(k)} &= \sum_{i=1}^{k} \left[\frac{1}{2} z_{(i-1)}^{2} \left(A_{1}^{(i-1)} - A_{1}^{(i)} \right) + z_{(i-1)} \left(A_{2}^{(i-1)} - A_{2}^{(i)} \right) \right] \\ B_{2}^{(k)} &= \sum_{i=1}^{k} \left[\frac{1}{3} z_{(i-1)}^{2} \left(A_{1}^{(i-1)} - A_{1}^{(i)} \right) + \frac{1}{2} z_{(i-1)}^{2} \left(A_{2}^{(i)} - A_{2}^{(i-1)} \right) \right] \\ B_{3}^{(k)} &= \sum_{i=1}^{k} \left[\frac{1}{2} z_{(i-1)}^{2} \left(A_{3}^{(i-1)} - A_{3}^{(i)} \right) + z_{(i-1)} \left(A_{4}^{(i-1)} - A_{4}^{(i)} \right) \right] \\ B_{4}^{(k)} &= \sum_{i=1}^{k} \left[\frac{1}{3} z_{(i-1)}^{3} \left(A_{3}^{(i)} - A_{3}^{(i-1)} \right) + \frac{1}{2} z_{(i-1)}^{2} \left(A_{4}^{(i)} - A_{4}^{(i-1)} \right) \right] \\ B_{5}^{(k)} &= \sum_{i=1}^{k} \left[\frac{1}{2} z_{(i-1)}^{2} \left(A_{5}^{(i-1)} - A_{5}^{(i)} \right) + z_{(i-1)} \left(A_{6}^{(i-1)} - A_{6}^{(i)} \right) \right] \\ B_{6}^{(k)} &= \sum_{i=1}^{k} \left[\frac{2}{3} z_{(i-1)}^{3} \left(A_{5}^{(i)} - A_{5}^{(i-1)} \right) + z_{(i-1)}^{2} \left(A_{6}^{(i)} - A_{6}^{(i-1)} \right) \right] \end{split}$$

The homogeneous boundary conditions for the interlaminar shear stresses along the free edges are

$$\sigma_{xz}^{(k)}|_{x=0} = \sigma_{yz}^{(k)}|_{y=0} = 0 \tag{1.98}$$

As stated earlier, the constants φ , φ_1 , φ_2 , λ_1 , λ_2 , η , ψ_1 and ψ_2 are determined using the principle of minimum total complementary energy Π . For a thermo-elastic orthotropic material, the strain-stress tensor under thermal loading can be written in the form

$$\begin{bmatrix} \mathcal{E}_{xx} \\ \mathcal{E}_{yy} \\ \mathcal{E}_{zz} \\ \mathcal{E}_{yz} \\ \mathcal{E}_{xz} \\ \mathcal{E}_{xy} \end{bmatrix} = \begin{bmatrix} s_{11}^{(j)} & s_{12}^{(j)} & s_{13}^{(j)} & 0 & 0 & s_{16}^{(j)} \\ s_{12}^{(j)} & s_{22}^{(j)} & s_{23}^{(j)} & 0 & 0 & s_{26}^{(j)} \\ s_{13}^{(j)} & s_{23}^{(j)} & s_{33}^{(j)} & 0 & 0 & s_{36}^{(j)} \\ 0 & 0 & 0 & s_{44}^{(j)} & s_{45}^{(j)} & 0 \\ 0 & 0 & 0 & s_{45}^{(j)} & s_{55}^{(j)} & 0 \\ s_{16}^{(j)} & s_{26}^{(j)} & s_{36}^{(j)} & 0 & 0 & s_{66}^{(j)} \end{bmatrix} \begin{bmatrix} \sigma_{xx} \\ \sigma_{yy} \\ \sigma_{zz} \\ \sigma_{xz} \\ \sigma_{xy} \end{bmatrix} + \Delta T \begin{bmatrix} \alpha_{11t} \\ \alpha_{22t} \\ \alpha_{33t} \\ 0 \\ 0 \\ 0 \\ 0 \end{bmatrix}$$

$$(1.99)$$

For the case of an *n*-plied laminate with linear-elastic material properties under thermal loading, the complementary energy is

$$\overline{\Pi} = \sum_{j=1}^{n} \left(\frac{1}{2} \iiint_{\Omega^{(j)}} \underline{\underline{\underline{S}}}^{(j)} \underline{\underline{\underline{S}}}^{(j)} \underline{\underline{\underline{G}}}^{(j)} d\Omega^{(j)} + \iiint_{\Omega^{(j)}} \underline{\underline{\underline{\sigma}}}^{(j)T} \underline{\underline{\underline{\sigma}}}^{(j)} \Delta T^{(j)} d\Omega^{(j)} \right) = \text{Min}$$
(1.100)

where $\Omega^{(j)}$ denotes the volume of the *j*-th layer of the laminate, $\overline{\underline{\underline{S}}}^{(j)}$ is a symmetric off-axis compliance matrix, ΔT is the constant temperature change and $\underline{\overline{\alpha}}_t^{(j)}$ are the coefficients of thermal expansion. The components of Cauchy's stress tensor are given in the vector representation:

$$\underline{\sigma}^{(j)} = \left\{ \sigma_{xx}^{(j)} \quad \sigma_{yy}^{(j)} \quad \sigma_{yz}^{(j)} \quad \sigma_{xz}^{(j)} \quad \sigma_{xy}^{(j)} \right\}^{T} \tag{1.101}$$

Under the assumption of linear elastic material, the elastic parameters of the j-th layer are given by the compliance matrix $\underline{\overline{g}}^{(j)}$ and the compiled off-axis coefficients of thermal expansion $\bar{\alpha}_{+}^{(j)}$:

$$\underline{\underline{S}}^{(j)} = \begin{bmatrix} \overline{s_1}_{1}^{(j)} & \overline{s_1}_{2}^{(j)} & \overline{s_1}_{3}^{(j)} & 0 & 0 & \overline{s_1}_{6}^{(j)} \\ \overline{s_1}_{2}^{(j)} & \overline{s_2}_{2}^{(j)} & \overline{s_2}_{3}^{(j)} & 0 & 0 & \overline{s_2}_{6}^{(j)} \\ \overline{s_1}_{3}^{(j)} & \overline{s_2}_{3}^{(j)} & \overline{s_3}_{3}^{(j)} & 0 & 0 & \overline{s_3}_{6}^{(j)} \\ 0 & 0 & 0 & \overline{s_4}_{4}^{(j)} & \overline{s_4}_{5}^{(j)} & 0 \\ 0 & 0 & 0 & \overline{s_4}_{5}^{(j)} & \overline{s_5}_{5}^{(j)} & 0 \\ \overline{s_1}_{6}^{(j)} & \overline{s_2}_{6}^{(j)} & \overline{s_3}_{6}^{(j)} & 0 & 0 & \overline{s_6}_{6}^{(j)} \end{bmatrix}$$

$$(1.102)$$

$$\underline{\overline{\alpha}}_{t}^{(j)} = \left\{ \overline{\alpha}_{xxt}^{(j)} \quad \overline{\alpha}_{yyt}^{(j)} \quad \overline{\alpha}_{zzt}^{(j)} \quad 0 \quad 0 \quad \overline{\alpha}_{xyt}^{(j)} \right\}^{T}$$
(1.103)

Note that the elastic compliances \overline{s}_{ij} in an off-axis system may be transformed in terms of the values s_{ij} given in the on-axis system using the elementary tensor transformations as

$$\begin{split} \overline{s}_{11} &= s_{11}\cos^4\Theta + s_{22}\sin^4\Theta + \left(2s_{12} + s_{66}\right)\cos^2\Theta\sin^2\Theta \\ \overline{s}_{22} &= s_{11}\sin^4\Theta + s_{22}\cos^4\Theta + \left(2s_{12} + s_{66}\right)\cos^2\Theta\sin^2\Theta, \overline{s}_{33} = s_{33} \\ \overline{s}_{12} &= \left(s_{11} + s_{22} - s_{66}\right)\cos^2\Theta\sin^2\Theta + s_{12}\left(\sin^4\Theta + \cos^4\Theta\right) \\ \overline{s}_{13} &= s_{13}\cos^2\Theta + s_{23}\sin^2\Theta, \quad \overline{s}_{23} = s_{13}\sin^2\Theta + s_{23}\cos^2\Theta \\ \overline{s}_{16} &= 2\left(s_{11}\cos^2\Theta - s_{22}\sin^2\Theta\right)\cos\Theta\sin\Theta + \left(2s_{12} + s_{66}\right)\left(\cos\Theta\sin^3\Theta - \cos^3\Theta\sin\Theta\right) \\ \overline{s}_{26} &= 2\left(s_{11}\sin^2\Theta - s_{22}\cos^2\Theta\right)\cos\Theta\sin\Theta + \left(2s_{12} + s_{66}\right)\left(\cos^3\Theta\sin\Theta - \cos\Theta\sin^3\Theta\right) \\ \overline{s}_{36} &= 2\left(s_{13} - s_{23}\right)\cos\Theta\sin\Theta, \quad \overline{s}_{44} = s_{44}\cos^2\Theta + s_{55}\sin^2\Theta \\ \overline{s}_{45} &= \left(s_{55} - s_{44}\right)\cos\Theta\sin\Theta, \quad \overline{s}_{55} = s_{44}\sin^2\Theta + s_{55}\cos^2\Theta \\ \overline{s}_{66} &= 4\left(s_{11} + s_{22} - 2s_{12}\right)\cos^2\Theta\sin^2\Theta + s_{66}\left(\cos^2\Theta - \sin^2\Theta\right)^2 \end{split}$$

The coefficients of thermal expansion of the orthotropic material need to be transformed to the transformation rules as

$$\overline{\alpha}_{11t} = \alpha_{11t}\cos^2\Theta + \alpha_{22t}\sin^2\Theta, \qquad \overline{\alpha}_{22t} = \alpha_{11t}\sin^2\Theta + \alpha_{22t}\cos^2\Theta$$

$$\overline{\alpha}_{12t} = 2\cos\Theta\sin\Theta(\alpha_{11t} - \alpha_{22t}), \qquad \overline{\alpha}_{23t} = \overline{\alpha}_{13t} = 0, \qquad \overline{\alpha}_{33t} = \alpha_{33t}$$

A detailed evaluation of the complementary energy given by equation (1.86) is documented by Mittelstedt and Becker (2004b) based on mathematical optimization procedures outlined by Vanderplaats (1984). The distribution of stress field near the free corner of symmetric laminates consisting of four plies made of transversely isotropic carbon fiber-reinforced plastic was estimated by Mittelstedt and Becker (2004b). Each ply has a thickness of 0.5 mm, which leads to a total laminate thickness of 2.0 mm, and the plate is exposed to a uniform temperature rise of $\Delta T = 100 \text{K}$ (°F = K × 9/5 – 459.67). The interlaminar normal stress σ_{zz} is commonly considered to be the predominant cause for the onset of delamination. Figures. 1.17(a)–(c) show three-dimensional plots of the interlaminar stresses σ_{zz} over the region $0 \le x \le 2.0$ mm, $0 \le y \le 2.0$ mm, and z = 0.4 mm for orientation angles of the laminate plies $[0^{\circ}/90^{\circ}]$ -, $[0^{\circ}/60^{\circ}]$ - and $[0^{\circ}/30^{\circ}]$ symmetric laminates, respectively. These figures reveal distinct dependence of the interlaminar stress fields on the variation of the orientation angle. In the pure cross-ply

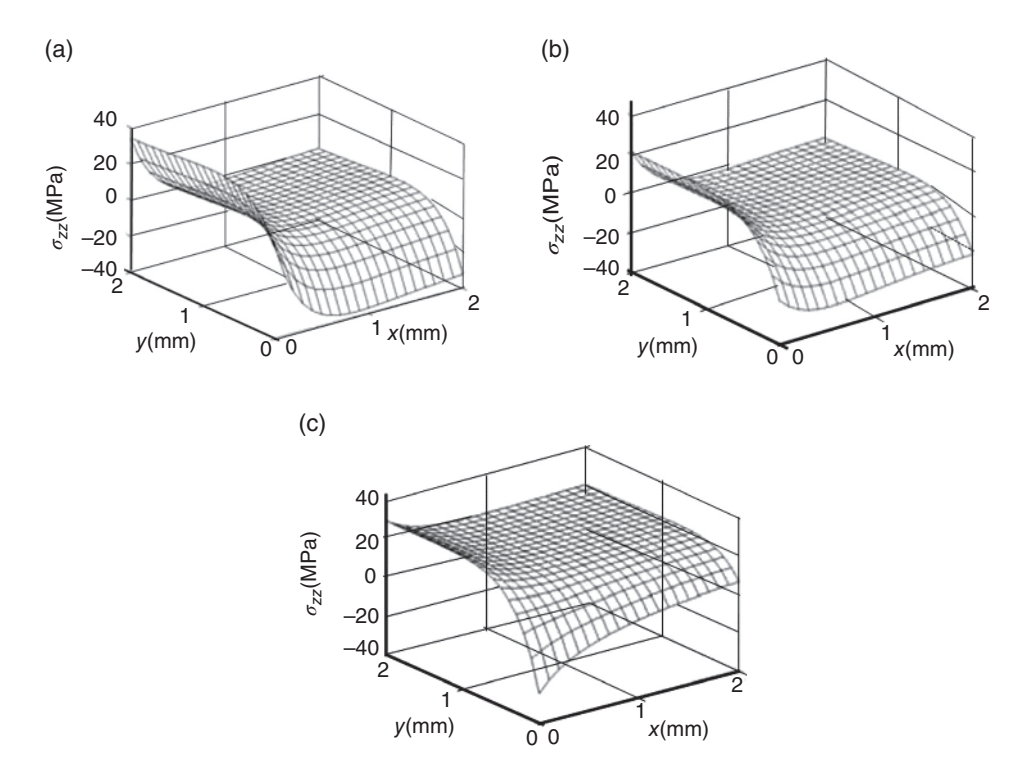


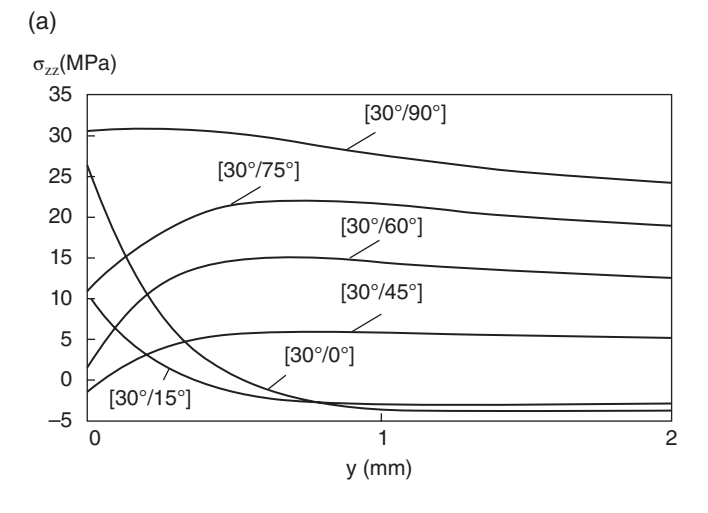
Figure 1.17 Interlaminar stress σ_{zz} over the plane xy for a uniform temperature rise of $\Delta T = 100$ K for: (a) $[0^{\circ}/90^{\circ}]$ -symmetric laminate, (b) $[0^{\circ}/60^{\circ}]$ -symmetric laminate, and (c) $[0^{\circ}/30^{\circ}]$ -symmetric laminate. (Mittlestedt and Becker, 2004b)

layup $[0^{\circ}/90^{\circ}]$ -symmetric laminates, the distribution of the peeling stress σ_{zz} is nearly perfectly symmetric with respect to the corner tip, i.e. the occurring stress fields along both in-plane coordinate directions x and y exhibit close similarities, with a reversed sign. After displaying some maximum value at the laminate edge, σ_{zz} changes its sign once before vanishing in the inner laminate regions. It is seen that the resultant distribution of the interlaminar normal stress σ_{zz} throughout the whole corner region of Figure 1.17(a) may essentially be constructed by the superposition of the two corresponding free-edge effects. Note that the highest tensile edge stresses σ_{zz} of all considered symmetric layups are encountered. This is to be expected since the mismatch in the elastic properties of the adjacent layers then also reaches its maximum, which is the primary reason for the occurrence of this class of stress concentration phenomenon. However, the situation changes with the [0°/60°]- and [0°/30°]-symmetric laminates shown in Figures. 1.17(b) and (c). With decreasing the second orientation angle, the resultant distributions of σ_{zz} lose their symmetry properties and the resultant free-edge effects display different behavior along their respective edges. This observation is easily explained with the differing material properties along the two laminate edges which, in all cases, is the basic reason for stress concentrations at the free edges of layered structures.

The dependence of the free-corner effect on the orientation angles of the laminate plies was further studied for the cases of $[30^{\circ}/\Theta_2]$ -symmetric laminates and $[60^{\circ}/\Theta_2]$ symmetric laminates by varying the fiber orientation Θ_2 . Figures. 1.18(a) and (b) show the distributions of σ_{zz} over the interval $0 \le y \le 2.0$ mm at x = 0.0 and z = 0.4 mm. It is seen from Figure 1.16(a) that the tensile stress σ_{zz} reaches its maximum value for the case of the [30°/0°]-symmetric laminate. For the case [30°/90°]-symmetric laminate the corner stresses remain higher than the free-edge stresses. On the other hand, the case of $[60^{\circ}/\Theta_2]$ -symmetric laminate, shown in Figure 1.17(b), reveals significant dependence of the resultant stresses on the angular orientation of the laminate plies.

1.7 Closing Remarks

This chapter has introduced the basic ingredients of the classical theory of fracture mechanics. The applications of this theory in aerospace and ocean structures will be considered in Chapter 2. Fracture mechanics criteria have their limitations, as described earlier. For example, one basic assumption in Irwin's linear elastic fracture mechanics is that the size of the plastic zone is small compared to the crack length. However, this assumption is quite restrictive for certain types of failure in steel materials, which are prone to brittle fracture and catastrophic failures. Furthermore, the *J*-integral is also limited for situations where plastic deformation at the crack does not extend to the furthest edge of the loaded part. The limitations of LEFM were discussed in detail by Bouchbinder et al. (2013). LEFM falls short of explaining the fast dynamics of a crack once it deviates from a perfectly straight path. Thus, high-velocity path instabilities, most notably the side-branching and the oscillatory instabilities, remain open problems in this framework. Furthermore, when fracture phenomena on a timescale for which inertial resistance of the material to motion is significant (i.e. hyperelasticity), the influence of crack tip plasticity and material strain rate sensitivity cannot be handled by



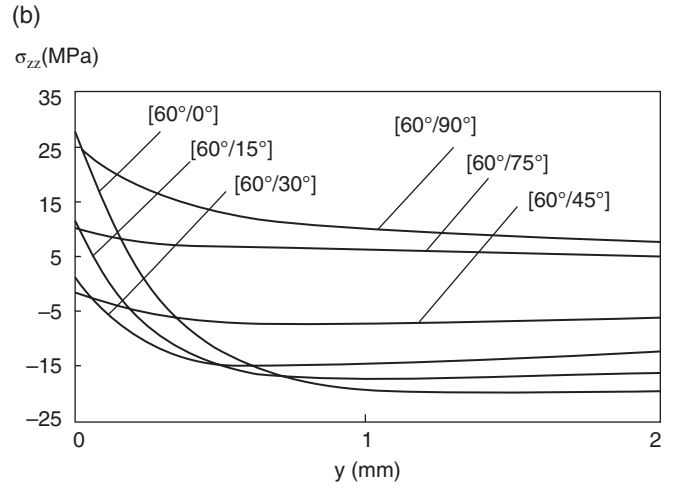


Figure 1.18 Interlaminar tensile stress σ_{zz} over the interval 0 < y < 2 mm, at x = 0 and z = 0.4 mm for a uniform temperature rise of $\Delta T = 100K$: (a) $[30^{\circ}/\Theta_2]$ -symmetric laminates and (b) $[60^{\circ}/\Theta_2]$ -symmetric laminates. Mittlestedt and Becker (2004b)

fracture mechanics theory. The importance of the *M*-integral will be demonstrated in dynamic fracture energy release due to interaction energy of mixed modes. These effects are only accounted for in the theory of dynamic fracture and peridynamics, which will be addressed in Chapter 3.

When a significant region around a crack tip experiences plastic deformation, other approaches can be used to determine the possibility of further crack extension and the direction of crack growth and branching. A simple technique, incorporated into numerical calculations, is the cohesive zone model method which is based on concepts proposed independently by Dugdale (1960) and Barenblatt (1962). The relationship between the Dugdale–Barenblatt models and Griffith's theory was first discussed by Willis (1967). The equivalence of the two approaches in the context of brittle fracture

was shown by Rice (1968). Interest in cohesive zone modeling of fracture was extended following the work of Xu and Needleman (1994) and Camacho and Ortiz (1996) on fracture dynamics.

The deterministic and stochastic modeling of fatigue crack damage in metallic structures for on-line diagnostics and health monitoring of operating machinery was considered by Patankar and Ray (1998) and Ray and Patankar (1998). A dynamical model of fatigue crack propagation was developed in the deterministic state-space setting based on the crack closure concept under cyclic stress excitation. The model state variables were crack length and crack opening stress. For the case of stochastic state-space model of fatigue crack propagation, the state-space model was found capable of capturing the effects of stress overload and underload on crack retardation and sequence effects. The non-stationary statistics of the crack growth process under (tensile) variable-amplitude load were obtained in a closed form without solving the governing stochastic differential equations of Itô's type. Teng et al. (2008) presented a statistical study on plasticity and fracture properties of a ductile aluminum casting. The test data fitted was found to fit well with both normal and Weibull probability functions. Shear fracture strains spread in a narrower range than tensile ones.

The theory of fracture mechanics does not account for corrosion and hydrogen embrittlement. However, some recent attempts have considered environment-assisted cracking, or environmentally induced cracking in the form of corrosion that produces a brittle fracture in alloys. These efforts will be discussed in Chapter 8.